Unveiling interfacial Li-ion dynamics in $Li_7La_3Zr_2O_{12}$:PEO(LiTFSI) composite polymer-ceramic solid electrolytes for all-solid-state lithium batteries

Mauricio R. Bonilla,[*,†] Fabián A. García Daza,[‡] Pierre Ranque,[¶] Frederic Aguesse,[¶] Javier Carrasco,[¶] and Elena Akhmatskaya[†,§]

†*BCAM - Basque Center for Applied Mathematics, Alameda de Mazarredo 14, E-48009 Bilbao, Spain*

‡*Department of Chemical Engineering and Analytical Science, The University of Manchester, Manchester M13 9PL, United Kingdom*

¶*Centre for Cooperative Research on Alternative Energies (CIC energiGUNE), Basque Research and Technology Alliance (BRTA), Alava Technology Park, Albert Einstein 48, 01510, Vitoria-Gasteiz, Spain*

§*IKERBASQUE, Basque Foundation for Science, Plaza Euskadi 5, 48009 Bilbao, Spain*

E-mail: mrincon@bcamath.org

Abstract

Unlocking the full potential of solid-state electrolytes (SSEs) is key to enabling safer and more-energy dense technologies than today's Li-ion batteries. In particular, composite materials comprising a conductive, flexible polymer matrix embedding ceramic filler particles are emerging as a good strategy to provide the combination of conductivity, mechanical and chemical stability demanded from SSEs. Yet, the electrochemical activity of these materials strongly depends on their polymer/ceramic interfacial Li-ion dynamics at the molecular scale, whose fundamental understanding remains elusive. While this interface has been explored for non-conductive ceramic fillers, atomistic modelling of interfaces involving a potentially more promising conductive ceramic filler is still lacking. We address this shortfall by employing Molecular Dynamics and enhanced Monte Carlo techniques to gain unprecedented insights into the interfacial Li-ion dynamics in a composite polymer-ceramic electrolyte, which integrates polyethylene oxide (PEO) plus $LiN(CF_3SO_2)_2$ lithium imide salt (LiTFSI), and Li-ion conductive cubic $Li_7La_3Zr_2O_{12}$ (LLZO) inclusions. Our simulations automatically produce the interfacial Li-ion distribution assumed in space-charge models and, for the first time, a long-range impact of the garnet surface on the Li-ion diffusivity is unveiled. Based on our calculations, tensile strength and ionic conductivity experimental measurements, we are able to explain a previously reported drop in conductivity at a critical filler fraction well below the theoretical percolation threshold. Our results pave the way for the computational modelling of other conductive filler/polymer combinations and the rational design of composite SSEs.

All-solid-state Li-ion batteries with a thin solid electrolyte material have the potential to revolutionize the energy-storage market by allowing the safe incorporation of a metal Li anode.[1,2] Indeed, the significant increase in energy density resulting from this paradigm could power the growth of several emerging applications, including long-range all-electric vehicles and large-scale wind and solar energy generation.[3]

Ceramics and polymers constitute the two main families of solid-state electrolyte materials. $Li_7La_3Zr_2O_{12}$ (LLZO) with the cubic garnet structure attracts increasing interest among ceramics due to its high conductivity at room-temperature (RT) and chemical compatibility with metallic Li.[4,5] However, ceramic electrolytes are brittle and provide poor intimate contact with the electrodes, leading to strong interfacial resistance, mechanical failure and dendrite formation.[6,7] Conversely, polymer electrolytes allow for better interface contact with the electrodes and mechanical stability during operation. Poly(ethylene oxide) (PEO)-based polymer electrolytes have been extensively studied and are already found in commercial batteries.[8] Yet, they often fail to prevent dendrite formation at high current densities, causing cell short-circuiting and battery failure.[9,10]

Composite SSE (CSSE) materials seek to integrate the benefits from both families by embedding ceramic particles (the filler) within an ion-conducting polymer phase. In particular, polyethylene oxide/Li-salt complexes (PEO(Li-salt)) embedding either inert (non ion-conducting)[11] or active (ion-conducting) oxide fillers, such as LLZO,[12,13] have been widely explored. Very recently, materials produced by in-situ polymerization onto porous inorganic skeletons have appeared that hold great promise for the incorporation into Li metal batteries.[14,15] Early works on CSSEs focused primarily on PEO(Li-salt) systems embedding inert nanoparticles.[16,17] Under certain circumstances, enhancement in RT conductivity at low filler contents ($\sim$ 5 - 10 % weight fraction, or $\sim$ 10 - 20 % volume fraction) was reported. These initial observations were rationalized by arguing that the addition of nanoparticles suppressed or dramatically slowed down the crystallization of the polymer matrix in the particle vicinity to promote the local mobility of the polymers.[18] However, some experiments indicated that conductivity enhancements in CSSEs could occur even at temperatures above the glass transition temperature, T_g, suggesting that additional mechanisms might be involved. Wieczorek et al.[19] applied the Lewis acid-base theory to explain the conductivity enhancement for acidic α-Al_2O_3 filled PEO electrolyte. They proposed that the strong affinity between ClO_4 and acidic groups on the surface of α-Al_2O_3 nano-oxides helped to separate the $Li^+ClO_4^-$ ion pairs, resulting in an increase in the concentration of free Li^+ ions. Ganapatibhotla and Maranas[20] experimentally found that the presence of acidic surface sites on α-Al_2O_3 nanoparticles did lead to an increase in the conductivity compared to non-acidic γ-Al_2O_3, even though no significant differences in polymer crystallinity existed between acidic and neutral Al_2O_3 nanoparticles. Similarly, it has been proposed that in CSSEs comprising pristine Li-ion conductive fillers such as LLZO or $Li_4Ti_5O_{12}$ (LLTO), similar surface enhancing effects may be at play. For example, the enrichment of the filler surface with Li-vacancies as a result of space charge effects (originating from the redistribution of Li^+ on both sides of the interface in order to equalize the electrochemical potential) may produce fast pathways for Li-ion conduction.[21,22] Another possible contributor to conductivity enhancement is partial decomposition of the active filler into Li-ion salts, as shown by Zheng and Yu[12] for LLZO:PEO(LiTFSI) CSSEs (LiTFSI = lithium bis(trifluoromethanesulfonyl) imide) through ^{6}Li NMR. More intriguing are the results by Choi et al.,[23] who reported a maximum in conductivity for LLZO:PEO($LiClO_4$) CSSEs occurring at 52 % wt LLZO for temperatures between 308 and 338 K. However, the relative increase in conductivity lowered as the temperature increased. On the contrary, Zagorski et al.[13] reported a monotonic decrease in conductivity with increasing LLZO concentration LLZO:PEO(LiTFSI) at 343 K (above $T_g \sim 336$ K), in agreement with what is expected if the reported RT conductivity enhancement at RT were exclusively the result of the filler-induced polymer amorphization. Evidently, synthesis history and the quality of particle dispersion in the polymer phase play a significant role in the measured trends. Therefore, accurate atomistic simulations of Li-ion transport in CSSEs incorporating idealized active fillers can shed light into the potential effect of interfacial Li-ion redistribution, surface vacancies, surface disorder and interfacial Li-ion exchange on Li-ion diffusion. Moreover, conducting such simulations above T_g allows disentangling these processes from those arising from changes in the polymer crystallinity.

Atomistic modelling of CSSEs is scarce and has focused exclusively on inert oxide particles. Molecular dynamics (MD) simulations of nano-Al_2O_3:PEO($LiBF_4$) CSSEs show a monotonic decrease on the ionic mobilities with particle loading above T_g.[24,25] In contrast, space-charge modelling of oxide nanoparticles embedded in PEO(Li-salt) complexes predicts a maximum in RT conductivity at $\omega = 16$ %[22,26] for both inert and active nanoparticles, in line with some of the experiments referred to above. We note, however, that in continuous and kinetic Monte Carlo models, space-charge enhancement is assumed *a priori* and thus, it is impossible to disentangle it from that due to crystallinity changes in the polymer phase. So far, force field - based atomistic modelling of CSSEs with active fillers are entirely lacking.

In this work we provide the first atomistic perspective on the interfacial Li-ion dynamics in CSSEs embedding active filler particles. The fact that Li^+ ions coexist in both phases and may undergo interfacial exchange makes this system distinctly different to those involving inert fillers.[24,25] Ebadi et al.[27] recently investigated the Li-metal:PEO(LiTFSI) interface using MD. However, accurate modelling of Li^+ exchange is beyond traditional MD for this particular system, given the chemical nature of Li plating. Conversely, interfacial Li-ion exchange in LLZO:PEO(LiTFSI) is a physical process (there are no redox interactions) and thus it is amenable to examination through classical force fields.[28] Here, we combine classical MD with a novel enhanced hybrid Monte Carlo technique to enable more efficient interfacial equilibration,[29,30] a challenging task that is often achieved by the freezing of interfacial atoms[31] or annealing schemes.[32] We focus on a relatively easy to fabricate CSSE, LLZO:PEO(LiTFSI), which provides an attractive ionic conductivity above T_g (or in the presence of plasticizer)[12,33] but has been fully overlooked from a fundamental, atomistic standpoint. In addition, we perform tensile strength and ionic conductivity measurements on the actual CSSE as a function ω to support some of our key theoretical conclusions.

Methods

Force Field

The interatomic potential for LLZO was calculated as a sum of Coulomb and Buckingham interactions, as reported in our recent work.[34] For the PEO chains, the Optimized Potentials for Liquid Simulations (OPLS)[35] was used to describe bonded and non-bonded interactions, as well as the interatomic interactions with the Li^+ ions.[36] The interaction parameters for the $TFSI^-$ anion were extracted from the force field for ionic liquids developed by Ködermmann and co-workers,[37] but a scaling factor of 0.55 was applied to the charge of nitrogen atoms to ensure electroneutrality in the LiTFSI molecule. For both PEO and TFSI$^-$, non-bonded potentials were the sum of Coulomb and Lennard-Jones (LJ) interactions. Thus, the cross PEO/TFSI$^-$ interaction parameters were obtained using the Lorenz-Berthelot rules. The cross parameters for PEO/LLZO and TFSI$^-$/LLZO are less well-defined, as the functional form of potentials employed differ. To obtain them, we rewrote the Buckingham-type interactions in an LJ functional form, following the strategy described in Section S1 of the SI.

Although the OPLS force field for PEO and that reported by Köddermann et al.[37] for TFSI$^-$ anions can accurately reproduce density, structural and transport properties, few authors have simulated the combined PEO, TFSI$^-$ and Li$^+$ system using non-polarizable atomistic models (see e.g. Brooks et al.[38]). Hence, we validated our force field for PEO(LiTFSI) by comparing the estimated mass densities (at 358 K and several LiTFSI contents) and ionic conductivities (at 358 K and 343 K) with available experimental and computational data. Details and results of these calculations are described in Section S2 of the SI.

Validating the force field for the composite LLZO:PEO(LiTFSI) system is considerably more difficult, given the lack of microscopic experimental data that can unequivocally explain the structural and dynamical features at the garnet polymer/garnet interface. Our results, however, are in good qualitative agreement with the experimental data on Li$^+$ transport from Zagórski et al.[13] and automatically produces a Stern-like interfacial layer predicted and indirectly measured by Brogioli et al.,[39] as we shall demonstrate below.

Simulation Details

We used two simulation methods in this study: MD and the generalized shadow hybrid Monte Carlo (GSHMC) method.[29] The GSHMC is a generalized hybrid Monte Carlo (GHMC) importance sampling scheme[40] where sampling is performed with respect to modified Hamiltonians, whilst sampling efficiency is increased by alternating short MD trajectories with MC stochastic sampling. The efficiency of GSHMC over traditional hybrid Monte Carlo methods lies in the possibility of preserving dynamical information and reaching higher acceptance rates. On the other hand, compared to MD, GSHMC offers a more rigorous control of the temperature and broader sampling due to its stochastic nature. GSHMC is implemented in MultiHMC-GROMACS,[30,41,42] an in-house modified version of the open-source package GROMACS 4.5.4.[43] Tunable parameters of GSHMC were adapted from our previous work on substituted LLZO garnets[34,44] and included the length of MD trajectories ($L = 250$), the time step ($\Delta t = 2$ fs), the partial velocity update parameter ($\phi = 0.1$) and the order of the modified Hamiltonian (4th order). In this work, we combined GSHMC with our two-stage Modified Adaptive Integration Approach (MAIA)[30] for modified Hamiltonian MC methods, which allowed for further sampling enhancement without time-step deterioration. For MD, we used a standard Velocity Verlet integrator with the time step $\Delta t = 2$ fs.

Simulations were performed at 343, 450, and 600 K. While at the lowest and highest temperatures only short polymer chains with $N = 10$ EO units were studied to accelerate the convergence of Li^+ transport to Fickian diffusion,[38] at 450 K polymers with $N = 10, 15, 20, 25, 30$ and 60 were considered as well. GSHMC was employed for system equilibration, while MD was used during production runs.

We introduced Ga^{3+} (0.15 per formula unit) into the Li^+ sublattice of LLZO, a common and effective way to stabilize the cubic garnet below 600 K.[34,44] All the initial configurations were generated with Packmol.[45] The simulation boxes contained $3 \times 3 \times 3$ LLZO supercells with 1416 Li atoms, 648 La atoms, 432 Zr atoms, 2592 O atoms, and 32 Ga atoms. In addition, the system included 88 LiTFSI molecules for a fixed PEO content corresponding to the experimental target concentration[13] EO:Li = 20:1. At 600 K, we also simulated EO:Li = 48:1, 32:1, 20:1, 16:1 and 11:1 to analyze Li^+ adsorption on the garnet surface. While the PEO and LiTFSI molecules were randomly located in the simulation box, the initial configuration of the LLZO garnet was obtained using the random sampling technique described elsewhere.[34,44] Periodic boundary conditions and van der Waals interactions with a cut-off distance of 12 Å were considered. Coulomb electrostatics were evaluated via the smooth particle mesh Ewald method with a cut-off radius of 11 Å.

The LLZO:PEO(LiTFSI) systems were equilibrated for 10 ns in the NVT ensemble first and then in the NPT ensemble. Temperature and pressure were controlled using a velocity rescaling thermostat (coupling time constant 0.1 ps) and the Parrinello-Rahman method[46] (coupling time constant 2 ps) at a target temperature and pressure $P = 1$ bar, respectively. All production runs were performed for 150 ns. Bond lengths with hydrogen atoms where constrained using the LINCS algorithm.[47]

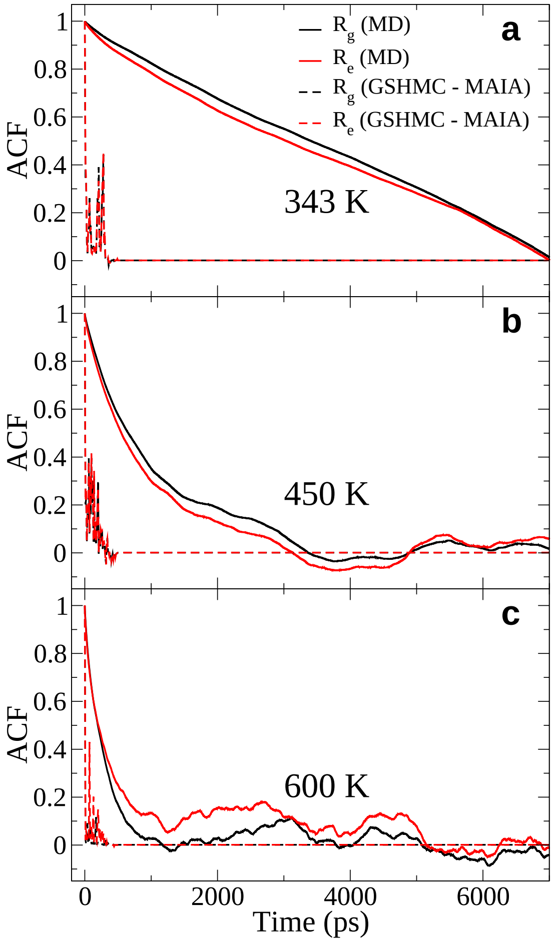

Figure 1: Comparison of the ACF obtained with MD (solid lines) and GSHMC (dashed lines) methods at (a) 343 K, (b) 450 K, and (c) 600 K for $N = 10$ EO monomers per chain. Black and red lines represent the ACF of the radius of gyration, R_g, and the end-to-end distance, R_e, of PEO polymers, respectively.

Figure 1 depicts the autocorrelation functions (ACF) for the end-to-end distance (R_e) and radius of gyration (R_g) for MD and GSHMC simulations at 343 K, 450 K, and 600 K during the equilibration stage in the NVT ensemble for systems with $N = 10$. The faster the ACF vanishes, the higher the average frequency with which uncorrelated samples are generated (i.e., the higher the sampling efficiency). Clearly, GSHMC provides significantly better sampling performance than MD. In order to quantify it, Section S3 of the SI provides the time normalized integrated ACF for $N = 10$ and $N = 60$ at 343 K, 450 K, and 600 K. GSHMC exhibits a sampling performance up to 145.5 times better than MD for the examined system.

Synthesis of cubic-LLZO

Ga-substituted LLZO ($Li_{6.55}Ga_{0.15}La_3Zr_2O_{12}$) was synthesized using a citric acid-nitrate route.[48,49] Ga_2O_3 ($\geq$ 99.99 %, Sigma Aldrich), $La(NO_3)_3$ ($\geq$ 99.99 %, Sigma Aldrich), $Zr(C_5H_7O_2)_4$ ($\geq$ 98 %, Alfa Aesar), and $LiNO_3$ ($\geq$ 99.0 %, Sigma Aldrich) were mixed in stoichiometric quantities (with a 10 % Li excess) and dissolved in a citric acid solution with a few drops of HNO_3. The organic components were then burned off at 600 °C for 12 h. The resulting powder was ground and reheated to 800 °C for 12 h in dry O_2 to obtain a pure cubic phase. The final material was ball milled to obtain Ga-LLZO particles of 1.4 μm in average, and was readily used for the elaboration of the composite membrane.

Preparation of Polymer Electrolyte Membranes

All free-standing polymer electrolytes were obtained by solvent casting and slurries were mixed via magnetic stirring to avoid any degradation of the starting materials, as described in Zagórski et al.[13] The compositions selected for this study were 10, 20, 30, 40 and 50 vol. % of LLZO (equivalent to 31, 51, 64, 73 and 80 wt. % respectively) dispersed in PEO:LiTFSI at a 20:1 ethylene oxide units per lithium ions ratio. PEO (MW = 5M, Sigma Aldrich), LiTFSI (99.95 %, Sigma Aldrich) and LLZO were mixed in ACN (99.8 %, Sigma Aldrich) during 12h. The resulting homogeneous slurries were casted in a PTFE evaporating dish. The membranes were formed and dried by subsequent solvent evaporations at RT (24 h) and dynamic vacuum (12 h at 50 °C). All these preparations were done in an argon filled glovebox under dry conditions.

X-ray diffraction

As-prepared LLZO was finely ground for powder X-Ray diffraction (PXRD) measurements. The powder was placed in an air-tight sample holder and measured from 15 to 80 ° in the two-theta angle using a Bruker D8 diffractometer mounted with a non-monochromated Cu source. The X-ray diffractogram is shown in Figure S4 of the SI, confirming that its structure corresponds to that of the cubic garnet when produced under the synthesis conditions described above (see ref. 50).

Tensile strain mechanical tests

Uniaxial stress-strain measurements were realized on previously cut membrane strips of 40 × 5 mm^2. The samples were fixed to a Universal Mechanical Testing Machine (Instron), then a tensile strain of 5 μm s^{-1} was applied until reaching a maximum value of strain of 20 % and the membrane elongation followed. Three measurements were performed for each membrane composition and the most representative result was selected. The Young's modulus was calculated from the slope of the linear part of the stress-strain curve.

Electrochemical measurements

Ionic conductivities of these composite electrolytes were determined by electrochemical impedance spectroscopies (EIS), in CR2032 coin cells. All cells were assembled in an argon-filled glove box (MBraun < 1ppm O2, H2O), using stainless steel discs as blocking electrodes. EIS measurements were done on a VMP3® potentiostat (BioLogic Science Instruments), from 1 MHz to 1 Hz, with an alternating current amplitude of 10 mV, in the temperature range from 25 to 80 °C. Resulting spectra were analyzed with EC-lab software.

The LLZO:PEO(LiTFSI) system

Figure 2a presents a snapshot of the equilibrated simulation box for the LLZO:PEO(LiTFSI) CSSE, at 450 K and for short olygomeric PEO chains with degree of polymerization $N = 10$ (the actual length of the simulation box was truncated to facilitate visualization). The garnet was cleaved to the center of the simulation box, creating two interfaces perpendicular to the x axis. In all cases, we considered the (100) plane of LLZO with differently exposed terminations on each side in the initial configurations (see Figure 2b). The surface concentrations and corresponding net charge density is reported in Table 1. The number of highly charged Zr^{+4}, La^{+3} and Ga^{+3} ions on the right interfacial plane (R.P.) is higher than that on the left interfacial plane (L.P.), producing a significantly higher surface charge density. This leads to considerable differences in the ionic distributions upon equilibration, most particularly for Li_g^+ (i.e., Li^+ originating in the garnet) and O^{2-}. Indeed, our simulations predict the formation of an amorphous ~ 3 Å interfacial monolayer of Li_g^+ ions arising upon interaction with PEO(LiTFSI), generating an unstructured but stable collection of surface Li-sites. This is shown in the density profile for Li_g^+ in the CSSE (solid red line in Figure 2c), depicted together with the corresponding equilibrium density profile for Li_g^+ in stand-alone LLZO (dotted black line) under periodic boundary conditions (PBC). The amorphous Li_g^+ surface layer is contained within the gray band on both interfacial planes in Figure 2c. It can be identified as the excess shoulders in the Li_g^+ distribution (for the CSSE) on the L.P. and R.P. with respect to the density profile for Li_g^+ under PBC (a similar monolayer can be identified for O^{2-} - not shown). The development of this layer is in agreement with ^{6}Li NMR analysis of LLZO:PEO(LiTFSI) and LLZO:PEO($\mathrm{LiClO_4}$),[12,51] which revealed a distribution of interfacial Li_g^+ distinctively different from that in the bulk crystal. Using first principle calculations, Canepa et al.[52] found a significant reconstruction of surface Li^+ and O^{2-} layers for tetragonal LLZO. Thus, it is not surprising to detect a higher degree of reconstruction in the more disordered cubic polymorph.

Notice that for $-16.5 < x < 16.5$ Å, the location of peaks and valleys for the Li_g^+ -

CSSE and Li_g^+ - PBC density distributions coincide. The magnitudes are not the same, however, because the simulation times do not allow every Li_g^+ ion to traverse the garnet, impeding the theoretical distribution of Li-site occupancies to be exactly fulfilled at each site. Nonetheless, the matching of features indicates that within $-16.5 < x < 16.5$ the garnet in the CSSE preserves the bulk structure. This is further confirmed by the total charge density distribution $q_{\mathrm{tot}}(x)$ illustrated in Figure 2d, which takes into account all atomic charges in the system. Here, the solid red line represents the equilibrated CSSE system, whilst the dotted line represents the LLZO under PBC. In the interval $-16.5 < x < 16.5$ Å, the charge distributions $q_{\mathrm{tot}}(x)$ - CSSE and $q_{\mathrm{tot}}(x)$ - PBC coincide very well. The net surface charge density for $a < x < b$, $Q_{a,b}$ is given by $\int_a^b q_{\mathrm{tot}} dx$. In the bulk region, we find that Q_{Bulk} is zero. Moreover, the charge between adjacent points of maxima in $q_{\mathrm{tot}}(x)$ for the CSSE and PBC garnet systems, Q_{osc} (see Figure 2c), is also zero within the bulk region. However, while the first charge oscillations outside the bulk region on both sides (cyan band in Figure 2d) have no net surface charge for the LLZO - PBC system (as expected), they have a negative net surface charge in the LLZO - CSSE system. The reason becomes clear after examining this same region in the density profiles represented in Figure 2c: the absence of a Li_g^+ peak for the LLZO - CSSE system within the cyan band (which is present in the LLZO - PBC system) indicates the existence of a Li_g^+-poor layer adjacent to the L.P and R.P. The nature of this layer can be ascribed to space-charge effects and will be discussed shortly.

Finally, Figure 2c shows that the last two peaks on the L.P. and R.P. (marked with * and **) differ. This can be attributed to the different terminations in the initial configuration (see Figure 2b and Table 1). Peak * on the L.P is significantly more pronounced than that on the R.P., due to the lower surface charge density arising from the lower concentration of highly charged ions (Zr^{+4}, La^{+3} and Ga^{+3}) on the L.P. The distribution of atoms in the PEO(LiTFSI) phase is also affected. The magenta line in Figure 2c, representing the density profile for oxygen atoms in the PEO chains, reveals minor (but non negligible) differences on each side of the interface. Interestingly, the polymer can interpenetrate the O^{2-}/ Li_g^+

monolayer (gray band, Figure 2c), which means that lithium ions in this region can also be coordinated by polymer oxygens. We shall see that this allows keeping electroneutrality, despite the unidirectional Li-ion influx towards the garnet. Importantly, the features described so far are common to all CSSE systems, regardless of temperature, PEO chain length or LiTFSI concentration.

Table 1: Initial distribution of exposed ions on the left and right planes of the garnet slab shown in Figure 2a.

ion	surface content, L.P. (nm^{-2})	surface content, R.P. (nm^{-2})
La^{3+}	0.657	1.709
Zr^{4+}	0.789	1.578
Ga^{3+}	0.066	0.0
O^{2-}	4.733	7.100
Li^{+}	4.339	3.681
surface charge density (e nm^{-2})	0.19+	0.92+

PEO binding on the LLZO surface

Some experiments on PEO use methyl-terminated chains, whereas others use hydroxyl-terminated chains (see, for instance, ref 53). We focused exclusively on hydroxyl-terminated chains, as they interact more strongly with the garnet (See Section S4 of the SI) and provide better insights into the effect of garnet/polymer interactions on the diffusive behavior of Li^+.

Figure 3a shows that, regardless of N, there are two prominent binding peaks extending $\sim$ 10 Å into the polymer phase, indicating that a significant part of the bound chains remains detached.[54] Our simulations reveal two distinct polymer binding mechanisms: (1) strong hydrogen bond-type interactions between the terminal OH group of the PEO chain and the surface oxygens of the garnet, and (2) weaker van der Waals (vdW) interactions between polymer oxygens and surface cations. The binding mechanisms are visualized in Figure 3b by means of the radial distribution function (RDF), between selected polymer atoms at the interface ($-25 < x < -20$ Å or $20 < x < 25$ Å) and garnet ions, at 450 K for a polymer

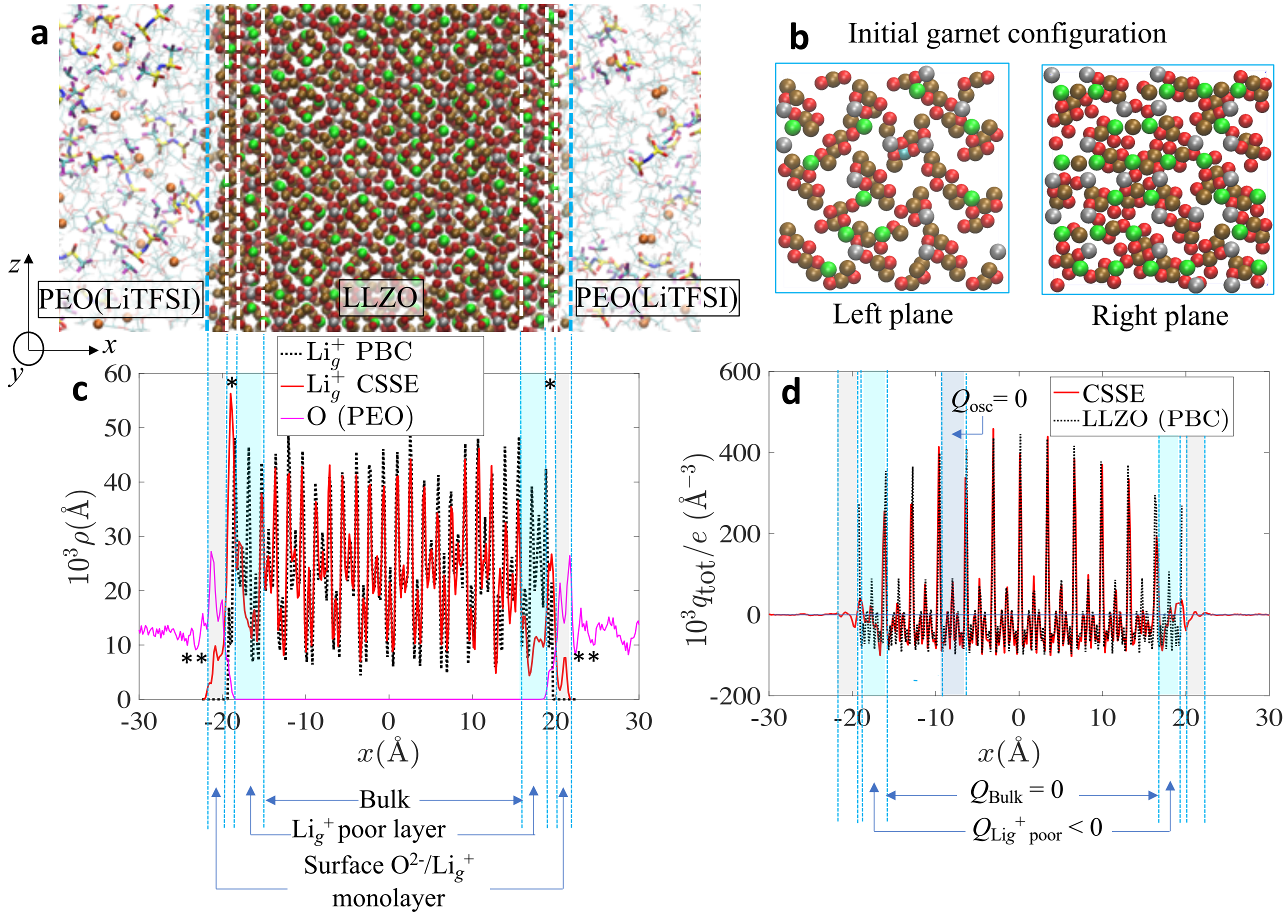

Figure 2: (a) The simulation box for the LLZO:PEO(LiTFSI) system, at 450 K and for short PEO chains with $N = 10$ EO monomers. The garnet is cleaved to the center of the simulation box, creating two interfaces perpendicular to the x axis. Brown, red, green, silver and white spheres within the garnet correspond to Li_g^+ (Li^+ ions originating in the LLZO), O^{2-}, Zr^{4+}, La^{3+} and Ga^{3+} ions, respectively. Only the -C- (cyan) and -O- (red) bonds in the PEO chains are shown, while those bonds with hydrogen are excluded for clarity. Li_p^+ (Li^+ ions originating in the LiTFSI salt) are depicted as orange spheres, while the bonds in the TFSI^- anions are shown in yellow (-S-), red (-O-), blue (-N-), cyan (-C-) and magenta (-F). (b) Initial distribution of exposed ions on the left and right planes of the garnet side of the LLZO:PEO(LiTFSI) interface. (c) Axial density distribution $\rho(x)$ for Li_g^+ in the equilibrated CSSE (solid red line), in stand-alone LLZO under PBC (dotted black line) and for the O atoms in the PEO polymer chains (solid magenta line) in the equilibrated CSSE. (d) Total charge distribution in the CSSE and stand-alone LLZO under PBC, $q_{\text{tot}}(x) = \sum_i q_i \rho_i(x)$. Here, q_i is the force-field charge of species i, and ρ_i its axial density profile.

length $N = 60$ (analogous results were obtained for other N values). Here, O_1 and H_1 denote the terminal O and H atoms in the PEO chain, while O_2 represents intermediate oxygen atoms. The sharp peak at 1.5 Å in the H_1 - O^{2-} RDF (black line) and the smaller

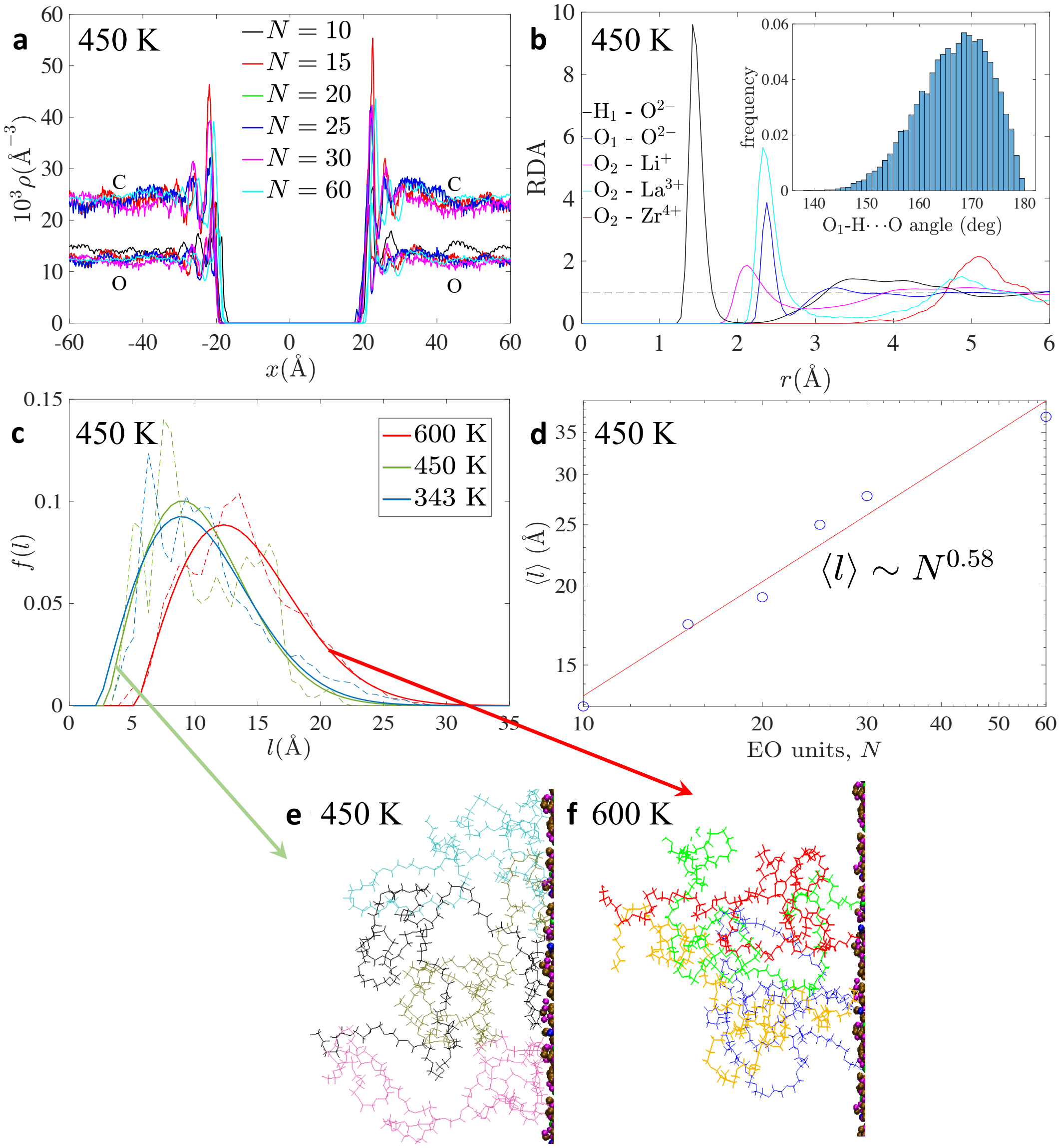

Figure 3: (a) Number density profile for PEO carbon and oxygen atoms, for several chain lengths N, at 450 K. The density profiles remain similar, with significant binding peaks within ~ 10 Å into the polymer phase from the garnet surface (the garnet is located in the interval $-22 < x < 22$ Å). (b) RDF between several pairs of polymer atoms and surface garnet ions for $N = 60$ chains (see main text for definitions of H_1, O_1 and O_2). The H_1-O^{2-} peak at 1.5 Å (black) and the subsequent O_1-O^{2-} peak at 2.4 Å (blue) are indicative of hydrogen bonding. This is further confirmed by the highly directional interaction, as derived from the O_1-H $\cdots$ O^{2-} angle distribution in the inset. Another significant binding interaction comes from vdW attraction between O^{2-} and exposed La^{3+} (in cyan). (c) Probability density distribution of adsorbed polymer extensions perpendicular to the garnet surface, l, at several temperatures for $N = 10$. The solid line is the best fit to a Rayleigh probability density function. (d) Variation of $\langle l \rangle$ with N at 450 K. (e,f) Snapshots of bound polymer configurations at 450 K and 600 K, respectively. Each chain is colored differently to facilitate following its contour. The hydrogen bond is strong enough to allow binding of the polymer termination at 600 K. At 450 K, interactions between intermediate polymer atoms and surface garnet atoms become stable.

peak at 2.4 Å in the O^{2-} - O_1 RDF (blue line) are telltale signs of hydrogen bonding. Further evidence comes from the O_1-H $\cdots$ O^{2-} angle distribution, depicted in the inset of Figure 3b. The angle remains above 120° and is on average 168°, which is indicative of the highly directional interaction, typical of strong hydrogen bonding.[55] Another significant peak appears at 2.4 Å in the O_2 - La^{3+} RDF (cyan line), making this specific interaction the main driver of binding mechanism 2. The higher abundance of exposed O^{2-} and La^{3+} on the R.P. of the LLZO particle explains why the binding peaks in Figure 3a are more pronounced at the right hand side. The overall shape of the density profiles is, nonetheless, very similar on either side of the interface.

A lower, broader peak is observed in the O_2 - Li^+ RDF (magenta line) at 2.2 Å, indicating that the contribution to polymer adsorption from O_2 interactions with Li^+ is relatively minor. Interestingly, the large Zr^{4+} ions do not interact as strongly as La^{3+} with the polymer O atoms (red line), despite their large formal charge and the fact that the La^{3+} and Zr^{4+} abundances are similar on the L.P. and R.P. (see Figure 2b and Table 1). This suggests that the impact of Coulomb forces is outweighed by vdW interactions. The RDF of other polymer - garnet atom pairs do not display any important features indicative of binding.

In order to determine how far bound chains can extend into the polymer phase perpendicularly to the LLZO surface, we estimated the probability distribution for the maximum extensions in the x direction for bound polymer chains (perpendicular to the garnet surface), l, for $N = 10$ at several temperatures (Figure 3c). We defined bound polymer chains as those for which one or more O_2 and/or H_1 atoms remained within 2.5 Å from the garnet surface (as indicated by the location of the main peaks in the RDF) within the interval $(t_s - 30, t_s)$, where t_s was the total simulation time (in ns). This time-frame was found to be adequate to allow for initially unbound chains to diffuse and bind to the garnet surface. The solid line represents the best fit to a Rayleigh probability density function. The distribution is shifted by 3.0 Å to the right at 600 K with respect to those at 450 K and 343 K, indicating a lower degree of polymer flattening (due to binding) at the highest temperature. This is the result of having both binding mechanism 1 and 2 present at and below 450 K (Figure 3e), and only binding mechanism 1 operating at 600 K (Figure 3f). The similarity between the $f(l)$ curves at 450 K and 343 K suggests that the distribution of polymer trains does not change significantly between these two temperatures. Note that the strong O_1-H $\cdots$ O^{2-} hydrogen bond leads to a binding behavior akin to that of grafted polymer.

Figure 3d shows that $\langle l \rangle$ varies with N as $\langle l \rangle \sim N^{0.58}$ at 450 K. This is likely to hold at 343 K (just above $T_g \sim 335$ K),[13] based on the similarities described above. As follows from the theoretical treatment by Alexander[56] and de Gennes,[57] as well as from more recent molecular simulation studies,[58] there are two possible regimes for a polymer grafted on an otherwise non-adsorbing surface. At low densities (LD), the bound polymer behaves much like a collection of isolated chains in solution (the so-called mushroom regime[59]), tracing out a hemisphere of Flory radius:

$$\langle l \rangle_{\mathrm{LD}} = aN^{0.6}, \tag{1}$$

where a is a proportionality constant of the order of the persistence length l_p. At high densities (HD), grafted polymer chains compete for binding sites and acquire a brush-like configuration (the brush regime[59]), with $\langle l \rangle_{\mathrm{LD}} \sim N$. Thus, at the investigated polymer matrix density (1.1 g$\cdot$cm^{-3}, typical of PEO-based CSSEs[13,60,61]), the bound polymer appears to follow the behavior of dilute, grafted PEO chains (equation 1). Mogurampelly and Ganesan[24,25] found that PEO($LiBF_4$) polymer electrolytes complexes containing non-conducting 1.4 nm Al_2O_3 nanoparticles displayed a monotonic decrease in ionic conductivities and mobilities with increasing filler content, most likely due to a reduced segmental dynamics of the polymer chains bound to the nanoparticles. This reduction in polymer mobility extended only a few angstroms into the polymer phase. However, when the particle diameter considerably exceeds the polymer length, the available surface area for binding is large enough to allow for the formation of a "polymer shell" around the filler particle $\sim l_p N^{0.6}$ thick in the mushroom regime, which means that the drop in the segmental dynamics can reach far into the polymer phase. Before exploring this argument in depth and its crucial relationship to Li-ion diffusion, we shall first show that long-range Li-ion transport occurs exclusively through the polymer phase, while the LLZO acts effectively as an adsorbent of polymer lithium ions, Li_p^+.

Lithium distribution

Figure 4a depicts the equilibrium density profiles of Li-ions originally located inside the garnet (Li_g^+, solid red line), within the PEO(LiTFSI) phase (Li_p^+, dotted green line), and oxygen atoms in the TFSI^- anions (O_3, dashed black line) at 450 K and $N = 10$. An analogous plot for $N = 60$ is presented in Figure 4b. For both values of N, the following important features are observed:

(*i*) There are Li-ion depletion regions in the PEO(LiTFSI) side of the interface (yellow band) and garnet side of the interface (blue band), the latter already identified in Figures 2c and 2d. Notice that no O_3 depletion is observed within the yellow band, indicating that this behavior is exclusive to the salt cation. And

(*ii*) There is a negligible amount of Li_g^+ in the PEO(LiTFSI) phase, but there is adsorption of Li_p^+ in the garnet.

Let us first consider feature (*i*). Recently, Brogioli et al.[39] modelled Al-doped LLZO: PEO(LiClO_4) using the Gouy-Chapmann-Stern equations. They assumed the existence of a Li-ion free layer (the so-called Stern layer) and a Li-ion vacancy-rich layer in the polymer and garnet sides of the interface, respectively, analogous to the blue and yellow bands indicated in Figures 2c and 2d. Their model was able to reproduce the experimental variation of interfacial resistivity with salt concentration, imposing assumptions on the Li-ion distribution that our simulations generate as a matter of course. Nevertheless, according to our simulations, space charge effects in the PEO(LiTFSI) phase are weak. Figure 4c depicts $q_{\mathrm{tot}}(x)$ around the Stern layer (yellow band) for the $N = 10$ system (the results are very similar for $N = 60$). $q_{\mathrm{tot}}(x)$ appears significantly flat within the Stern layer and into the polymer phase, as compared with the interfacial region. Closer inspection, however (see

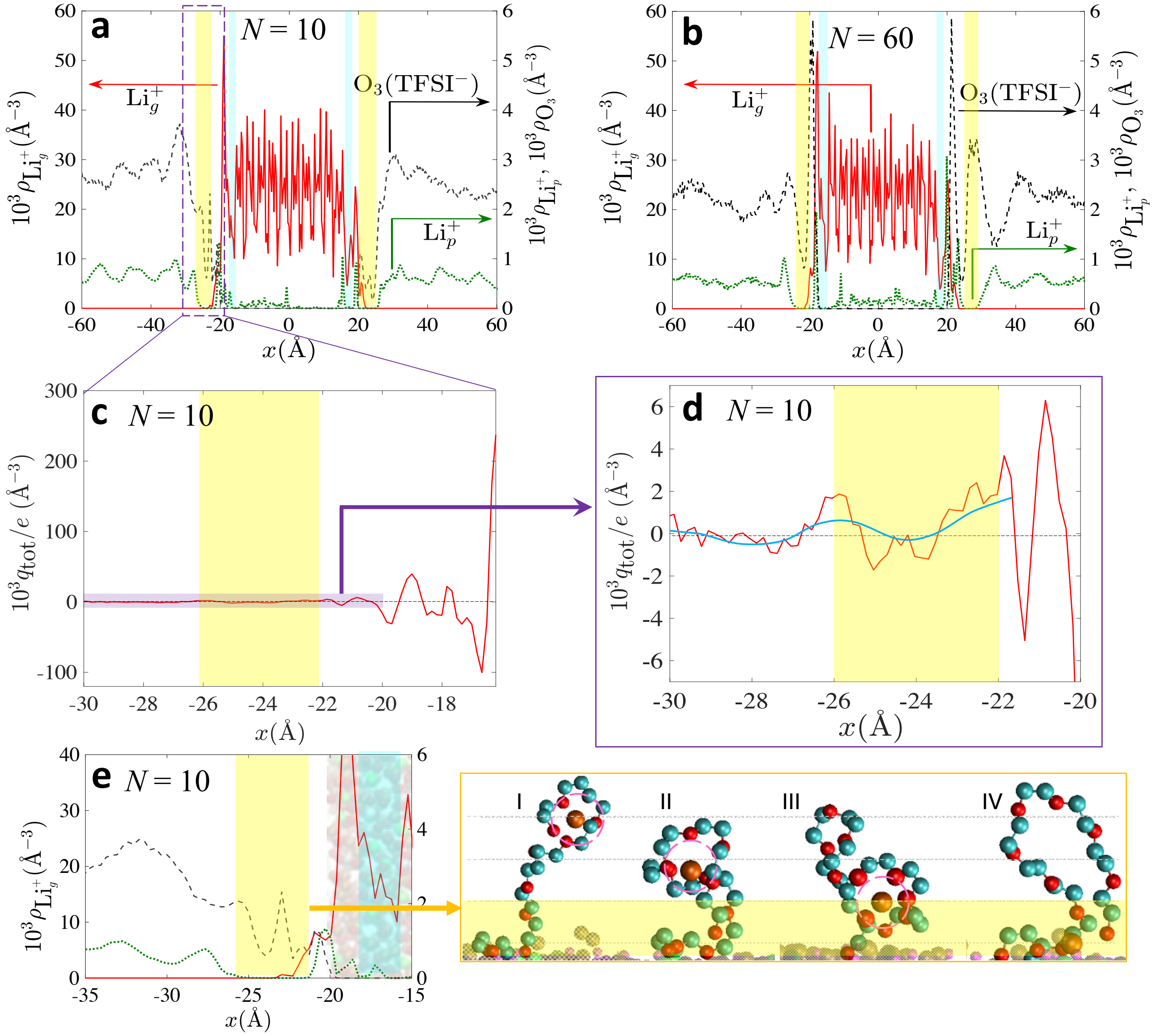

Figure 4: Number density profiles of Li_g^+ (solid red), Li_p^+ (dotted green) and O_3 (dashed black) ions, for a polymer phase comprised of $N = 10$ (a) and $N = 60$ (b) PEO chains at 450 K. Cyan and yellow bands represent the Stern layer (in the polymer phase) and Li-ion poor layer (in the garnet phase), respectively. Notably, there is no Li_g^+ in the PEO(LiTFSI), indicating unidirectional Li-ion exchange. (c) Charge density distribution in the polymer side of the (left) interface for $N = 10$ at 450 K. (d) Close-up of the region indicated in (c). The blue line represents a moving average curve (taking a window size of 1 Å) up until the end of the Stern layer (where the LLZO surface begins). (e) Left: close-up of (a) around the 4.5 Å thick Stern layer. Right: snapshots of a four-steps intrachain diffusion of Li_p^+ along an adsorbed polymer chain at 450 K and $N = 10$. The chain must fold in order to allow for Li_p^+ coordination, restricting the motion of Li_p^+ along the polymer chain, which occurs in $\sim$ 4.5 Å length steps (dotted lines are a guide to the eye). This generates a Li-ion free zone in the density profile of Li_p^+ (i.e. the Stern layer).

Figure 4d), reveals that for $-30 < x < -22$ Å, $q_{\text{tot}}(x)$ tends to increase with x, as expected in the Gouy-Chapmann-Stern model. For $x < -30$, $|q_{\text{tot}}(x)| \leq +1$ eÅ^{-3} and its average is zero. Analogous behavior is detected on the right side of the interface.

We showed that a net neutral "bulk region" exists within the garnet in the interval $-16.5 < x < 16.5$ Å at 450 K (see Figure 2d). Given also the neutrality of the PEO(LiTFSI) phase for $x < -30$ or $x > 30$ Å, it is obvious that the interfaces are also neutral thanks to the space charge effects automatically generated by our simulations.

Brogioli et al.[39] determined that the interfacial resistance to Li-ion diffusion depended primarily on the thickness of the Stern layer (estimated to be just a few angstroms wide) and suggested that it was an activated energy barrier, but could not pinpoint its origin. Figure 4e (left) contains a close-up of the left side Stern layer in Figure 4a, revealing that its thickness is ~ 4.5 Å. The same thickness is found on the right side and for $N = 60$, indicating that its nature is independent on the polymer length. We explain its origin, dimensions and the negligible amount of Li_g^+ in the PEO(LiTFSI) phase (feature (*ii*)) as follows:

Earlier MD simulations revealed a three-steps mechanism for the diffusion of Li_p^+ through the PEO matrix: (a) intrachain Li-ion hopping along the polymer backbone, (b) cooperative Li-ion motion coordinated with the PEO segments, and (c) Li-ion inter-segmental hopping from one chain to the other.[62–64] Throughout these steps, Li_p^+ is coordinated by 4 - 5 polymer O atoms.[62,65] Because a Li_p^+ ion is often coordinated by O atoms from a single chain, this chain must fold in order to allow for such degree of O coordination (see Figure 4e (right)). Brooks et al.[38] showed that while the jumping distance is temperature dependent, the most frequent distance in the 360 - 450 K range is approximately that between adjacent polymer oxygens in bulk PEO(LiTFSI) (~ 2.5 Å). However, restrictions in chain folding imposed by the garnet surface forces the jump required to transfer the Li_p^+ from the polymer phase to the garnet surface to be at least twice as long. This occurs because a bound chain is not infinitely flexible, but requires about one persistence length $l_p = 3.8$ Å[66] to acquire a significant curvature as it leaves the garnet surface. Away from the garnet surface, it is obvious that chain diffusion and mobility do not allow for intrachain hopping to be reflected on the density profile. However, the discrete nature of intrachain diffusion becomes clear near the surface through the formation a Li-ion free Stern layer. This is illustrated in Figure 4e (right), depicting the evolution of a Li_p^+ ion (orange) transferring from the PEO(LiTFSI) phase to the garnet through a four-steps intraparticle hopping process along a single $N = 10$ chain at 450 K (other chains are not shown for clarity). From steps (I)-(III), the Li_p^+ ion is coordinated by $\sim 4-5$ PEO Oxygen atoms (those intersecting the 3.0 Å radius[62] magenta circle). The fact that no Li-ions transfer from the garnet to the polymer phase suggests the existence of a steep energy barrier, which will be explored in future work.

Electroneutrality

Because electroneutrality must be kept, adsorption of Li_p^+ ions into the garnet bulk must lead to diffusion of Li_g^+ to the unstructured $\mathrm{O}^{2-}/\mathrm{Li}_p^+$ monolayer (gray band in Figure 2c). However, this does not provoke the uptake of Li_g^+ within PEO(LiTFSI) in atomistic time scales and thus, Li-ion exchange cannot contribute significantly to ionic conduction.

We now consider how Li ions (either Li_p^+ or Li_g^+) are stabilized at the interface. Figures 5a and 5b depict the RDF for interfacial Li - O at 450 K for $N = 10$ and $N = 60$, respectively. Here, the O atoms can originate in the garnet (O^{2-}), in the polymer (O_1, O_2) or in the TSFI^- anion (O_3). We consider the Li ions in a 1 Å bin next to the Stern layer (i.e., in the $\mathrm{O}^{2-}/\mathrm{Li}_g^+$ unstructured surface monolayer) at $|x| = 20$ Å and also at the beginning of the bulk region in LLZO, at $|x| = 15$ Å. In the bulk crystal, coordination of Li ions should be uniquely achieved by either 4 or 6 O^{2-} ions at an average distance of 2.1 Å from the central Li ion. Interestingly, the RDF at $|x| = 20$ reveals that the oxygen coordination shell has also a 2.1 Å radius. This tighter coordination shell at the garnet surface, compared to that in PEO(LiTFSI) may lead to the suggested energy barrier impeding Li-ion transfer from the garnet to the polymer. In this case, however, the O atoms in the shell can originate in the polymer phase. Indeed, figures 5c,d and 5e,c show the average oxygen coordination profile of Li ions for $N = 10$ and $N = 60$, respectively, between the O^{2-}/Li_g^+ monolayer and the LLZO bulk on both sides of the interface at 450 K. In all cases, total oxygen coordination numbers stay between sightly below 4 and 5, with those Li ions within 2 Å of the Stern layer more likely to be under-coordinated with respect to the polymer bulk. Nonetheless, past this point oxygen coordination numbers remain above 4 and tend towards ~ 5 in the bulk region, which is the average between the typical coordination of tetrahedral and octahedral Li-sites in the garnet. The blue band represents the Li-ion poor region identified in Figure 2c. Between this band and the L.P/R.P., there is penetration of PEO(LiTFSI) within the garnet phase, allowing O atoms from PEO and $TFSI^-$ help stabilize both Li_g^+ and adsorbed Li_p^+ within the interfacial garnet layers. Indeed, Figures 5c-f show that in the vicinity of the Stern layer, O_1, O_2 and O_3 contribute in average 2 coordinating oxygens. Expectedly, the most abundant O type, O_2, is the largest contributor to the coordination of interfacial Li ions from the PEO(LiTFSI) phase, while contribution from O_3 is minor. Moving towards the garnet bulk, PEO(LiTFSI) penetration fades and O^{2-} coordination takes over.

In summary, the mixed garnet/PEO(LiTFSI) oxygen coordination of Li-ions arising from phase interpenetration explains how some Li_p^+ can enter the bulk LLZO while forcing Li_g^+ onto the interface without violating electroneutrality.

Transport parallel to the interface

In order to investigate Li-ion diffusion parallel to the garnet surface in the polymer phase, we follow the formulation by Liu et al.,[67] briefly summarized below.

Let $N_{\{x_1,x_2\}}(t, t+\tau)$ be the number of particles that stay within the region $\{x_1, x_2\}$ in the $(t, t+\tau)$ period of time. The mean square displacement in the y direction inside $\{x_1, x_2\}$ is defined as

$$\langle y(\tau)^2 \rangle_{\{x_1,x_2\}} = \frac{1}{n_t} \sum_{t=1}^{n_t} \frac{1}{N_{\{x_1,x_2\}}(t,t)} \sum_{i \in N_{\{x_1,x_2\}}(t,t+\tau)} (y_i(t,t+\tau) - y_i(t))^2, \tag{2}$$

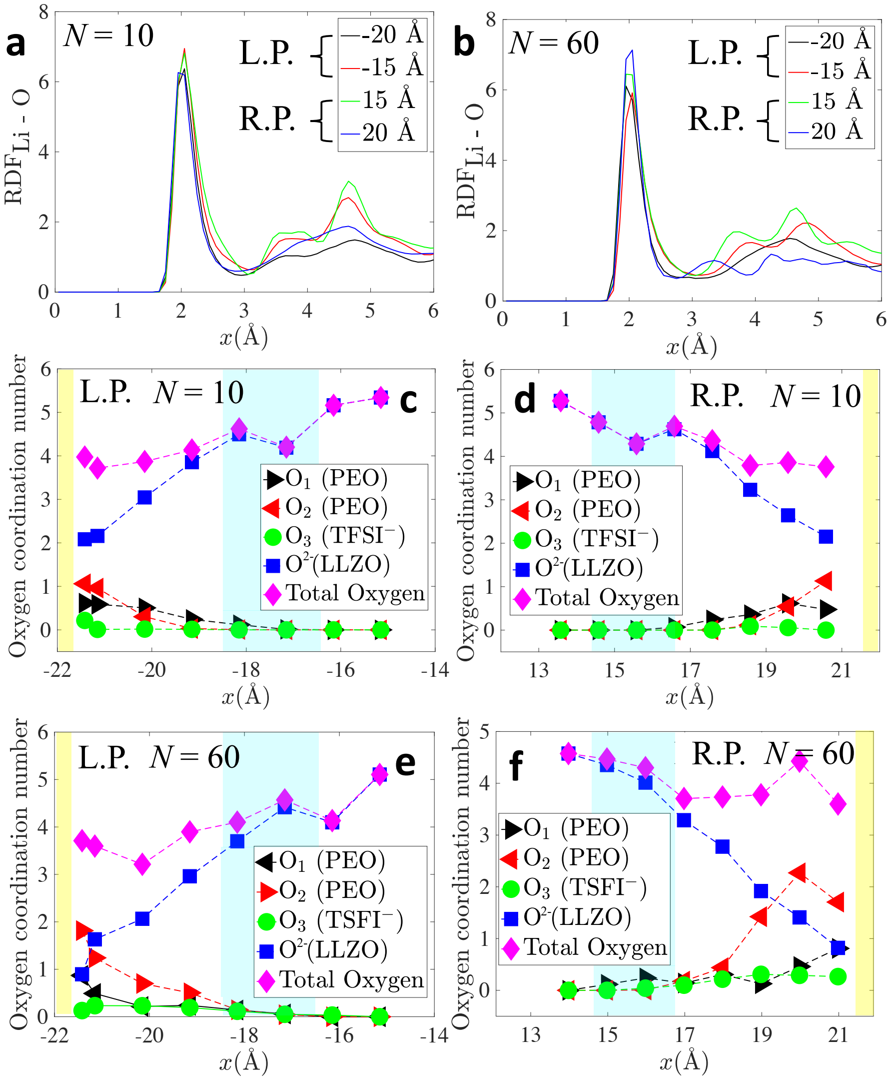

Figure 5: RDF for Li - O atoms within LLZO at 450 K for $N = 10$ (a) and $N = 60$ (b). We examine Li ions in 1 Å bins centered at $x = -20$ Å and $x = 20$ Å (the LLZO side of the interface) and Li ions in 1 Å bins centered at $x = -15$ Å and $x = 15$ Å (the garnet bulk). We consider O atoms originating in the polymer (O_1 and O_2), the salt anion (O_3) and the garnet (O^{2-}). (c-f) Average oxygen coordination profiles for Li-ions between the Stern layer (yellow band) and the garnet bulk, at 450 K for $N = 10$ ((c) left plane (L.P.), (d) right plane (R.P.)) and for $N = 60$ ((e) L.P., (f) R.P.). Individual contributions from each oxygen type are indicated, as well as the total oxygen coordination number. The blue band represents the Li-ion poor region within the garnet. The lines are a guide to the eye.

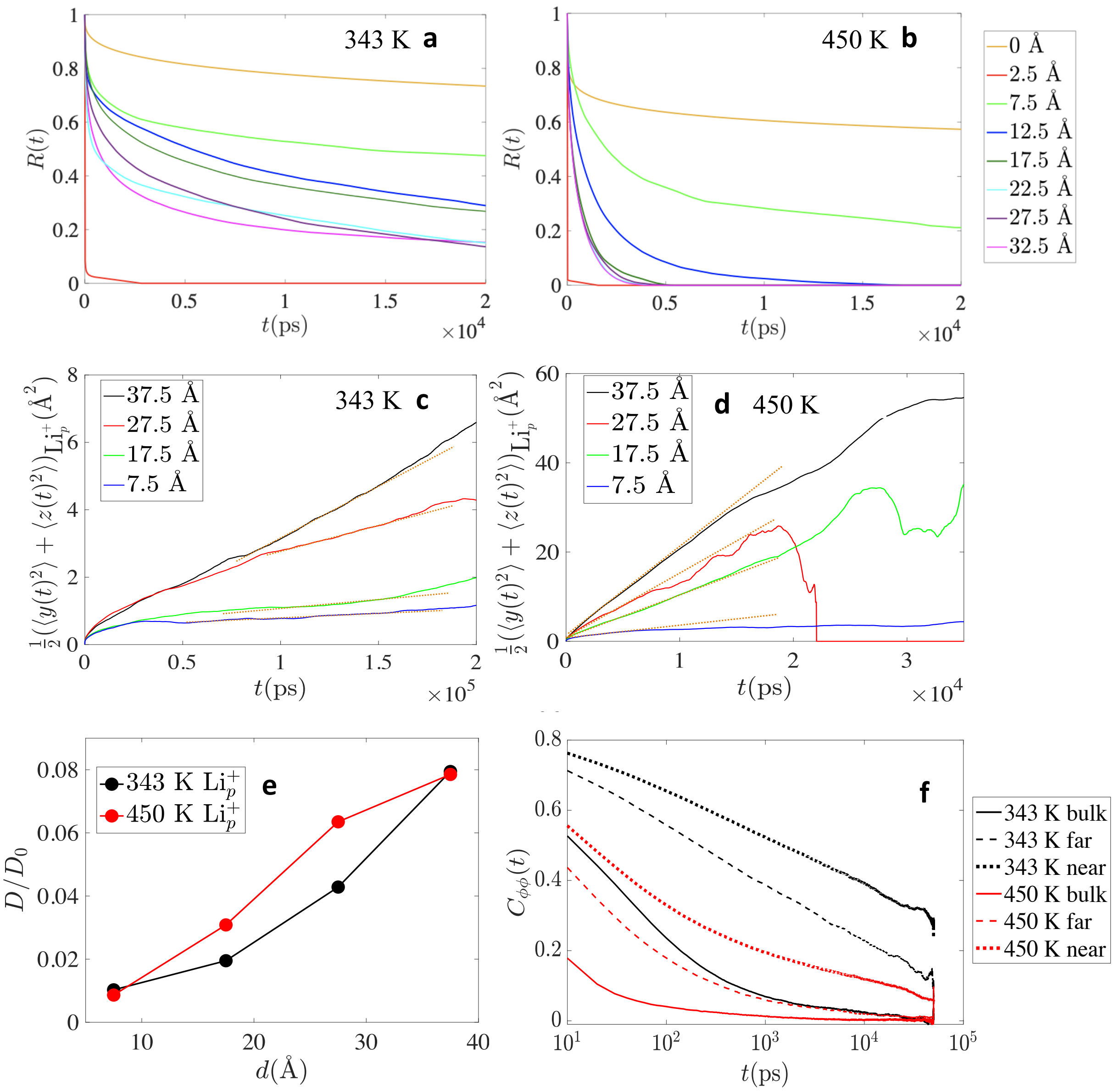

Figure 6: (a,b) Variation of survival rates, $R(t)$, of Li_p^+ ions with the distance from the garnet surface d at (a) 343 K and (b) 450 K. (c, d) y, z in-plane MSD for Li_p^+ ions at four values of d at 343 K (c) and 450 K (d). (e) Lateral diffusivity D (eq. 5) to bulk diffusivity D_0 ratio for Li_p^+ at 343 K and 450 K. (f) Autocorrelation function for the C–O–C–C dihedrals, $C_{\phi\phi}$, at 343 K (black) and 450 K (red) in the bulk (solid lines), for dihedrals "far" from the garnet surface in the composite system ($d < 20$ Å) (dashed-lines), and dihedrals "near" the surface in the composite system ($d < 10$ Å) (dotted lines).

where n_t is the total number of time steps averaged over. The survival rate $R(\tau)$, representing the average fraction of particles remaining for a period of at least τ within $\{x_1, x_2\}$ is

$$R(\tau) = \frac{1}{n_t} \sum_{t=1}^{n_t} \frac{N_{\{x_1,x_2\}}(t, t+\tau)}{N_{\{x_1,x_2\}}(t, t)}. \tag{3}$$

With the definitions above, the diffusion coefficient in y can be estimated from

$$D_{yy}(\{x_1, x_2\}) = \lim_{\tau \to +\infty} \frac{\langle y(\tau)^2 \rangle_{\{x_1,x_2\}}}{2\tau R(\tau)}, \tag{4}$$

and analogously for $D_{zz}(\{x_1, x_2\})$. The diffusion coefficient parallel to the interface is then calculated as

$$D = \frac{1}{2}(D_{yy} + D_{zz}). \tag{5}$$

Figures 6a and 6b depict the survival rate, $R(t)$ (eq. 3), for Li_p^+ ions at various values of the distance d from the garnet surface, at 343 K and 450 K for $N = 10$. The results are averages from both sides of the interface, which were found to differ by less that 10 % . The reported distances represent the midpoints of 5 Å thick bins for $d \geq 7.5$Å. For $d < 7.5$Å, the thickness of the bins is reduced to 3 Å. At any given d, $R(t)$ is expectedly higher at 343 K than at 450 K for every t, due to the enhancement of mobility with temperature. However, it is interesting to note that the relative order of the curves is the same at both temperatures. At the garnet surface ($d = 0$ Å, yellow line), the survival rate for adsorbed Li_p^+ ions is considerably higher than that at any farther distance. This indicates that a relatively small fraction of adsorbed Li_p^+ can diffuse towards the garnet bulk in atomistic time scales. At $d = 2.5$ Å (red line), $R(t)$ decays very quickly, because this area comprises the unstable Stern region. The rate of decay increases again at $d = 7.5$ Å, and decreases progressively as d increases, reaching an apparent equilibrium at 450 K. However, such an equilibrium is never actually reached in the parallel diffusivity, as we shall see below.

Figure 6e shows the ratio of the diffusion coefficient parallel to the interface, D (equation 5), to the bulk diffusion coefficient D_0 for Li_p^+ in the PEO(LiTFSI) phase for several values of d, averaging the results on both sides of the interface ($D_0 = 1.4 \times 10^{-7}\text{cm}^2/\text{s}$ and $3.3 \times 10^{-6}\text{cm}^2/\text{s}$ at 343 K and 450 K, respectively, as computed using our force field). The corresponding in-plane MSDs, $\frac{1}{2}(\langle y(t)^2\rangle + \langle z(t)^2\rangle)_{\{x_1,x_2\}}$ (eq. 2) for Li_p^+ are depicted in Figure 6c and 6d, along with the slope lines (solid orange lines) from which the parallel diffusivities were calculated (eq. 5). It is important to note that the in-plane MSD is only meaningful within the time frame for which $R(t)$ is still relatively high. To expand this interval, we divided the PEO(LiTFSI) phase into 4 larger bins, centered at the values of d specified in the figure legends. By doing this, we were able to identify regions of normal diffusion from which a reliable value of D can be drawn.

Surprisingly, the D/D_0 ratio in Figure 6e is over an order of magnitude below unity, regardless of d. That is, the presence of the garnet wall has a surprisingly long-range effect on the diffusivity of Li_p^+. This is in stark contrast with earlier findings from Mogurampelly and Ganesan,[24] who showed that small alumina nanoparticles (14 Å in diameter) embedded in PEO(LiBF_4) only impacted Li-ion diffusion within ~ 8 Å from the nanoparticles surface. In order to investigate the severe decline in D at all values of d, we estimated the segmental mobility of the polymer chains through the autocorrelation function of the C–O–C–C dihedrals, $C_{\phi\phi}$:[24]

$$C_{\phi\phi} = \frac{\langle cos\phi(t)cos\phi(0)\rangle - \langle cos\phi(0)\rangle^2}{\langle cos\phi(0)cos\phi(0)\rangle - \langle cos\phi(0)\rangle^2}. \tag{6}$$

It is well understood that a decrease in polymer segmental mobility originated from inert nanoparticle inclusions leads to reduced Li-ion diffusivity in PEO(Li-salt) composite systems.[24,68] Figure 6f shows the evolution of $C_{\phi\phi}$ for dihedrals "far" from the garnet surface ($d > 20$ Å), "near" the surface ($d < 10$ Å) and the corresponding bulk curves for PEO(LiTFSI) at 343 K and 450 K. $C_{\phi\phi}$ decays considerably slower near the surface than far away from it. This is a consequence of polymer binding and a significant reduction on the segmental degrees of freedom for the interfacial polymers. Nonetheless, $C_{\phi\phi}$ also decays considerably slower far from the interface when compared to the bulk $C_{\phi\phi}$ value. For small oxide nanoparticles ($<$ 20 Å in diameter) the polymer chains recover the bulk mobility 10

Å away from the nanoparticle surface.[24,68] Therefore, it is obvious that the filler particle size has a severe impact on Li-ion diffusion. In particular, LLZO particles that are large with respect to the PEO chain length are likely to lead to long-range reduction in polymer mobility and, consequently, to long-range reduction in the ionic diffusivities. In addition, we do not find that space charge effects lead to improvement of interfacial Li-ion transport, as suggested in other works.[22] The conditions under which a highly conductive interfacial layer is formed need to be investigated further. Below, we put forward the implications of these results in light of the possible formation of a "rigidified" polymer shell around the filler particles.

Understanding macroscopic conduction

Recently, Zagórski et al.[13] showed that in (Ga substituted) LLZO:PEO(LiTFSI) composites with micron sized filler particles, the conductivity drops very significantly, by over two orders of magnitude, between $\omega = 40$ % and $\omega = 50$ % at 343 K. Conductivity results from Zagórski et al.[13] are reproduced in Figure 7a. Below $\omega \sim 40\%$, the conductivity is close to that in bulk PEO(LiTFSI) and decreases slowly with increasing ω. These results agree well with our simulations, as we predict that the introduction of large LLZO particles is detrimental to Li-ion transport due to three major factors. First, high interfacial resistance (particularly for garnet-to-polymer Li-ion exchange) renders the particles essentially non-conducting. Second, the polymer chains surrounding the particle are significantly less mobile, reducing the ability of Li_p^+ to diffuse. And finally, the third factor is the absence of diffusion enhancement arising from space charge effects along the LLZO particle surface.

The sudden decrease in conductivity is reminiscent of a percolated network, in which spanning clusters of the most conductive phase (in this case, the matrix) cease to exist at a critical threshold ω_c. When non-overlapping conductive spheres are dispersed into an insulating continuum, a percolation threshold appears at $\omega_c \approx 29\%$.[69] However, when non-overlapping insulating spheres are dispersed into a conductive continuum, the ionic

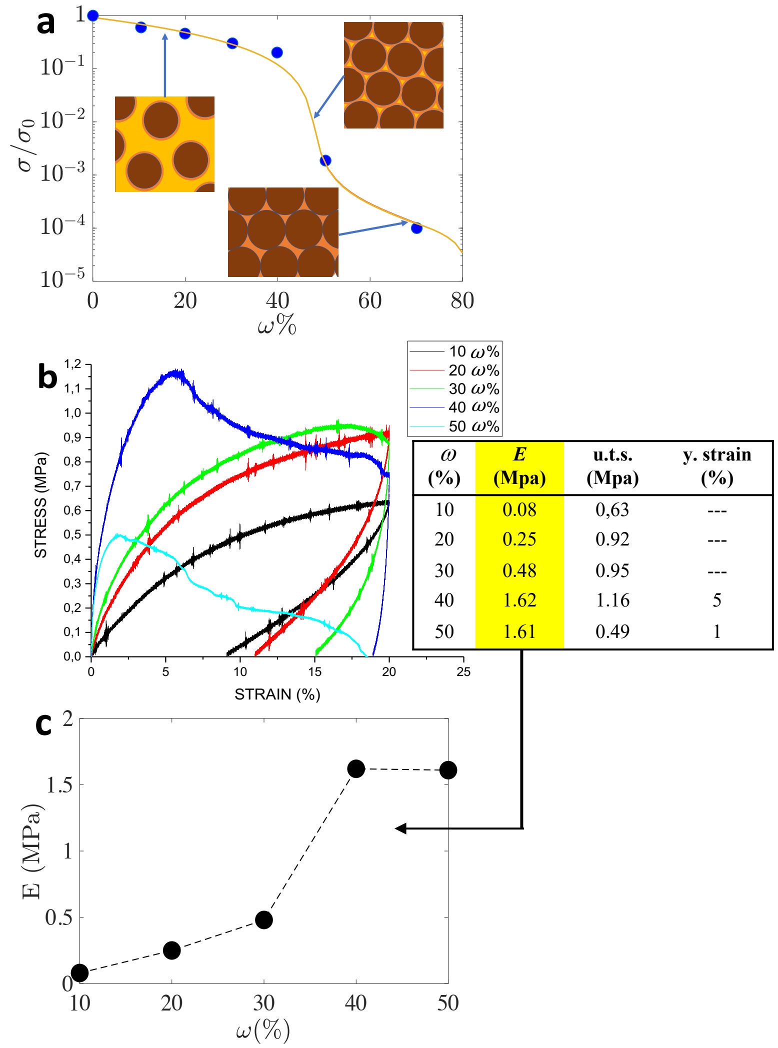

ω (%)	*E* (Mpa)	u.t.s. (Mpa)	y. strain (%)
10	0.08	0,63	---
20	0.25	0.92	---
30	0.48	0.95	---
40	1.62	1.16	5
50	1.61	0.49	1

Figure 7: (a) Symbols: relative conductivity σ/σ_0 (bulk conductivity $\sigma_0 = 10^{-3}$ S·cm^{-1}) as a function of filler volume fraction, ω, in LLZO:PEO(LiTFSI) composites at 343 K according to the work from Zagórski et al.[13] Solid line: best fit of equations (8)-(12) for $\delta/\tilde{R} = 0.10, 0.11, 0.12$ (the curves basically overlap). The insets depict the possible origin of a percolation effect manifesting from $\omega \sim 40$ - 50 %: the polymer shells surrounding the filler particles begin to overlap with one another. The chains in these shells are considerably less mobile and produce a long-range drop in Li_p^+ diffusivity. At very high ω, conduction occurs only through the shells and in-between the particles interstices. Adapted with permission from Zagórski et al.[13] Copyright (2019) American Chemical Society. (b) Stress-strain curves for LLZO:PEO(LiTFSI) at several values of ω measured experimentally in this work. There is a significant increase in the initial slope of the stress-strain curves at $\omega = 40$ % and $\omega = 50$ % with respect to $\omega < 40$ %, followed by plastic yield. The Young's modulus, E (extracted from the initial slope of the curve), ultimate tensile strain, u.t.s. (maximum stress before yield) and yield strain are reported in the table to the right. (c) Graphical representation of E, depicting the abrupt initial hardening of the composite at $\omega = 40$ %.

conductivity decreases approximately as a power law and conduction occurs well beyond random close packing ($\omega \approx 64\%$), because small ions can still diffuse through the interstitial space between the jammed spheres. This is known as Archie's law[70] and is routinely verified in conductive-brine filled porous rocks in the oil industry. In such system, a theoretical percolation threshold is predicted at $\omega \approx 97\%$,[71,72] well beyond the critical threshold observed in Zagórski et al.[13] data (see Figure 7a). Similarly, numerous models of permeability in multiphase media predict a smooth decrease in conductivity with ω for non-overlapping insulating spheres in a conductive continuum up to random close packing.[73] It is only when particles have an aspect ratio between 4 and 5, that a percolation threshold is theoretically predicted to appear in $40\% < \omega < 50$ %.[74] The particles employed in this work and those in Zagórski et al.[13] were approximately spherical and thus, this explanation is not feasible.

We propose an alternative hypothesis. Consider micron size garnet particles and high molecular weight PEO chains (MW=10^6 g·mol^{-1}, $N = 2.3\times10^4$), similar to those in Zagórski et al.[13] As a first approximation, let us assume that coefficient a in equation (1) has the ideal worm-like chain value for the bulk polymer

$$a = \sqrt{2} l_p^{2/5} (\frac{l_p}{l_d})^{\frac{1}{5}} l_b^{3/5}, \tag{7}$$

where l_b and l_d are monomer length and effective diameter, respectively, and l_p is the persistence length.[75] Taking $l_p = 3.8$ Å for PEO,[66] $l_b = 2.5$ Å (obtained from dividing the length of an extended chain by N) and $l_d = l_b$, we get $\langle l \rangle_{\rm LD} = 187$ nm. Thus, an isolated polymer chain bound to the garnet surface would cover a surface area $\sim \pi \langle l \rangle_{\rm LD}^2 = 0.11 \mu{\rm m}^2$, significantly below the available surface area on the particle ($\sim 3\mu{\rm m}^2$). This comfortably allows for the formation of the mushroom-like configuration shown in our simulations at $T \leq 450K$. For the PEO chains used in the experimental part of this work (MW= 5×10^6 g×mol^{-1}, $N = 4.4 \cdot 10^5$), $\langle l \rangle_{\rm LD} = 491$ nm, corresponding to a surface coverage of ~ 0.7 $\mu{\rm m}^2$ and allowing again for a mushroom-like configuration. A layer of mushroom-like polymer covering the particle surface would display significantly reduced segmental mobility in the vicinity of the particle surface, as shown by our simulations. This is due to the polymer chains binding the particle surface at several points across the chain length, as opposed to the more mobile brush-like configuration that is prevalent at 600 K (see Figure 3). Within this shell of "rigidified" polymer, it is reasonable to expect that Li-ion mobility is severely affected. Indeed, we have shown that the disruption in diffusion can be surprisingly long-range, even beyond one polymer chain length.

Because the polymer shells are soft and can overlap, a percolation threshold may now arise and a suitable percolation model can be employed to estimate the critical filler content and polymer shell thickness. We shall follow the theoretical treatment by Nan and Smith,[76] who determined the effective conductivity of the composite filler + shell particle, $\tilde{\sigma}$, through the Maxwell-Garnet mixing rule. The high surface resistance of the equilibrated LLZO particle means that, effectively, $\sigma_s >> \sigma_f$, where σ_s and σ_f denote the polymer shell and filler conductivities, respectively. In that case, the Maxwell-Garnet equation reduces the conductivity of the composite particle, σ_{fs}, to:

$$\sigma_{fs} = \frac{2(1-\tilde{\omega})}{1+\tilde{\omega}}\sigma_s, \tag{8}$$

where $\tilde{\omega}$ is the fraction of filler in the composite particle,

$$\tilde{\omega} = \frac{1}{(1+\delta/\tilde{R})^3} \tag{9}$$

and δ and $\tilde{R}$ are shell thickness and filler particle radius, respectively. Since the polymer shells can overlap, we can now use a suitable effective medium approximation to estimate the effective conductivity of the CSSE, σ_{eff}, as a function of ω. Kirkpatrick[77] extended the classical Maxwell-Garnett model by incorporating percolation theory, following:

$$\left(\frac{\omega}{\tilde{\omega}}\right)\frac{\sigma_{fs}-\sigma_{eff}}{\sigma_{fs}-(\frac{\omega_c}{\tilde{\omega}-\omega_c})\sigma_{eff}} + \left(1-\frac{\omega}{\tilde{\omega}}\right)\frac{\sigma_0-\sigma_{eff}}{\sigma_0-(\frac{\omega_c}{\tilde{\omega}-\omega_c})\sigma_{eff}} = 0, \quad \omega/\tilde{\omega} < 1, \tag{10}$$

where σ_0 is the conductivity of the polymer matrix.

When $\omega/\tilde{\omega} \geq 1$, the bulk polymer vanishes and all available PEO is "trapped" within the shells. Because the LLZO particles are rigid and cannot overlap, we may assume that the system does no longer percolate and equation (8) applies again in the form

$$\sigma_{eff} = \frac{2(1-\omega)}{1+\omega}\sigma_s, \quad \omega/\tilde{\omega} \geq 1. \tag{11}$$

Equations (10) and (11) alone tend to overestimate the conductivity, because they do not account for the increase in tortuosity τ for the ionic diffusion paths with increasing ω. Tortuosity can be significantly dependent on the system dimensions for finite size configurations,[78] such as thin electrolyte layers. For simplicity, however, we shall use the scaling relation $\tau = (1-\omega)^{-0.36}$ for infinitely large systems, assuming that the CSSE is conductive up to essentially $\omega = 1$.[79] In that case, the predicted conductivity in the CSSE is

$$\sigma = \frac{\sigma_{eff}}{(1-\omega)^{-0.36}}. \tag{12}$$

Equations (8) - (12) have three adjustable parameters: $\delta/\tilde{R}$, ω_c and σ_s. However, we impose that ω_c should occur beyond overlap of the randomly packed composite particles (i.e., $\omega_c/\tilde{\omega} > 0.64$) and that the percolation threshold in equation (10) complies with $\omega_c/\tilde{\omega} < 1$. After fitting the experimental data from Zagórski et al.[13] (Figure 7a), we obtain $\sigma_s \approx 10^{-3}\sigma_0$, $\omega_c = 0.48$ and $0.10 < \delta/\tilde{R} < 0.13$. The resulting fitting curves for $\delta/\tilde{R} = 0.10$, 0.11 and 0.13 are shown in Figure 7a. σ/σ_0 is clearly insensitive to variations in $\delta/\tilde{R}$ within this rather narrow range. The average filler particle size reported in Zagórski et al.[13] had a radius of 0.7 μm, which suggests a polymer shell $\sim$ 70 - 90 nm thick. Therefore, the experimental data is consistent with the existence of a highly resistive particle surrounded by a thin envelope of a poorly conductive polymer shell.

There are several important aspects to note. Firstly, the shell thickness is below our ideal estimate for the polymer mushroom thickness (187 nm). This could be interpreted as follows. For long polymer chains, the outer layers of the bound polymer mushroom may be mobile enough for bulk diffusion to be essentially reestablished. Therefore, the estimated shell thickness is relatively independent of N for sufficiently long chains. Secondly, σ_s/σ_0 is at least one order of magnitude below the estimated value of D/D_0 in Figure (6e) (D/D_0 measures the diffusivity in the polymer phase within 40 Å from the interface and, consequently, should constitute a measure of the diffusivity within the hypothesized polymer shell). Although the conductivity depends also on the anion diffusivity and thus, is not necessarily proportional to the cation diffusivity, changes in conductivity tend to be within the same order of magnitude as changes in Li-ion diffusivity (see Figure S5 in the SI). It is possible that beyond the percolation threshold, the overlapping shells are more densely packed and, as a consequence, the Li-ion diffusivity can decrease even more with respect to the bulk value.

To further explore our hypothesis, we carried out linear tensile strain tests on LLZO:PEO(LiTFSI) composites at several values of ω. The resulting curves are shown in Figure 7b, while the small strain Young's moduli obtained from the initial slopes of the curves are depicted in Figure 7c. Reinforcement of the polymer matrix with LLZO leads to a linear increase of the Young's modulus with ω up to $\omega = 30$ %, without noticeable variation on the elastic behavior of the material. However, a drastic increase in Young's modulus is observed at $\omega = 40$ %, while a yield stress appears at about 5 % strain. This change is accentuated at $\omega = 50$ %, with the Young's modulus remaining constant while the yield stress decreases to about 1 %. Therefore, a significant change in the microstructure takes place at around $\omega = 40$ %.

The effect of a polymer layer surrounding small filler particles has been discussed in the context of alumina nanoparticles in polymeric epoxy matrices by Vasileva and Friedrich.[80] It was found that an effective random close packing fraction of $\omega = 37$ % and a polymer shell thickness between 50 - 90 nm explained well their micromechanical data. Following a similar line of thought, one can infer that entanglement between overlapping bound polymer shells put in contact at values of ω approaching to ω_c increases mechanical strength at low strains, but leads to lower yield strains as the entanglement length between polymer chains becomes shorter and pockets of free, bulk polymer become disconnected. Further analysis is required to fully prove this hypothesis, but the coincidence between the sudden and significant increase in resistance to Li-ion transport and the increase of the Young's modulus appears unlikely to be fortuitous.

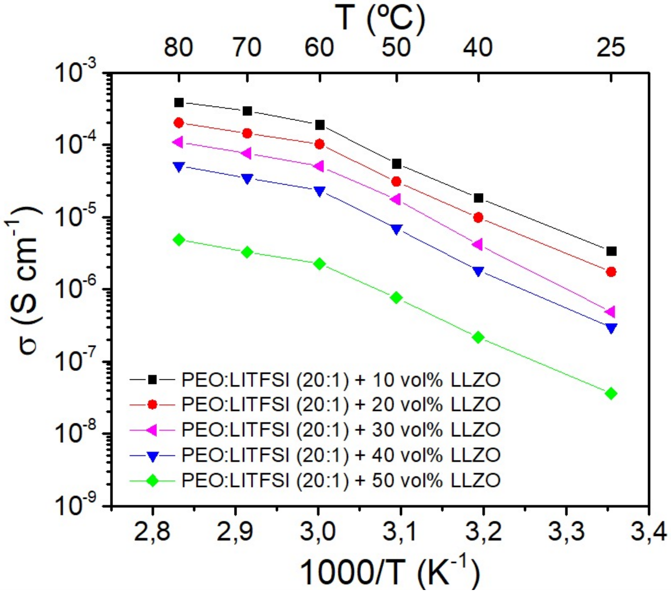

Figure 8: Arrhenius plots for the conductivity σ of the CSSE samples synthesized in this work, at the filler fractions of ω = 10, 20, 30, 40 and 50 %. Two activation energies are observed, with the inflection point located approximately at the glass transition temperature T_g.

Figure 8 depicts the Arrhenius plots for the conductivity of the CSSE samples fabricated for this study, at the filler fractions of ω = 10, 20, 30 , 40 and 50 %. Independently of the garnet content, there are two activation energies: 0.38 eV for $T > 60$ °C and 1.17 eV for $T < 60$ °C. The inflection point corresponds to the glass transition temperature of the polymer ($\sim$ 63 °C for pure PEO) and does not present any significant variation with ω. Clearly, the activation energy associated to Li-ion conduction is most strongly dependent on the polymer phase and decreases by a factor of $\sim$ 3 when the polymer transits from semicrystalline to amorphous phase. Interestingly, we observed the same trend described in Figure 7a at all temperatures: σ decreases monotonically with ω, but a significantly more abrupt decrease occurs between 40 % and 50 %. Previous work has indicated that a maximum in σ is observed in the RT conductivity of LLZO:PEO or LLTO:PEO systems at low volume fractions.[12,21,22] Zheng et al.[12] used micron size LLZO particles and found that the conductivity enhancement at RT was likely due to chemical decomposition of LLZO. In most other scenarios, the filler consisted in either nanoparticles or nanowires and thus, the higher available surface area was potentially more likely to allow for widespread polymer amorphization at RT, enhancing σ. Our measurements and simulations show that for micron size particles, the beneficial effect of filler-induced polymer amorphization is absent at 343 K (i.e. above T_g) and, if it does occur below T_g, it is located at $\omega < 10$ %. In addition, conductivity enhancement introduced by space charge effects may not truly occur. It is also possible that in systems comprising small nanoparticles, aggregation is considerably more challenging to avoid, prompting the presence of percolation effects that become hard to separate from the underlying physics of the system.

Conclusions

In summary, our atomistic simulations reveal that the PEO/LLZO interface of LLZO:PEO(LiTFSI) CSSEs displays an unanticipated molecular-level adaptability in optimizing bonding within the polymer in the presence of the garnet filler. First, we found that large portions of the PEO chains are detached from the garnet surface, with the presence of only few anchoring PEO-garnet points which are associated to the coexistence of strong hydrogen bonds and weak vdW interactions. Second, space-charge distribution at the PEO/LLZO interface forms an asymmetric Stern-like layer which, at atomistic time scales, allows for the uptake of Li ions within the PEO into the garnet but prevents the opposite ion flow. Finally, we also observed that the presence of the garnet severely diminishes ionic diffusivity in PEO even at large distances from the interface. Experimental measurements performed in this work show a dramatic change in the mechanical properties of the material at $\omega = 40$ %, approximately coinciding with a previously reported percolation threshold in the conductivity of LLZO:PEO(LiTFSI) CSSEs synthesized under identical conditions.[13] We have not seen this effect reported in LLZO nanoparticle systems (or any other conductive filler) for CSSEs, which we suspect is due to more effective agglomeration of bound polymer chains onto the surface of large microparticles. However, definitive conclusions can only be achieved through the systematic study of CSSE with different particle size distributions and a wide range of polymer lengths under identical manufacturing and testing conditions. We shall be following this line of inquiry in the future.

Supporting Information Available

Associated content: S1. Parameter adjustment for the Lennard Jones and Buckingham potentials associated with the PEO (LiTFSI) and LLZO phases, respectively. S2. Validation of the force field for PEO(LiTFSI) by comparing with experimental densities and conductivities. S3. Integrated autocorrelation function for LLZO:PEO(LiTFSI), sampled through the generalized shadow hybrid Monte Carlo technique and MD. S4. Analysis of the binding of capped PEO chains to the LLZO surface. S5. XRD of powder Ga-LLZO and variation of Li-ion diffusivity and conductivity with EO:LI ratio.

Data availability

The data that support the findings of this study are available from the corresponding author upon reasonable request.

Acknowledgement

We acknowledge the financial support by the Ministerio de Ciencia e Innovación (MICINN) of the Spanish Government through the Juan de la Cierva grant IJC2018-037214-I, PID2019-104927GB-C22, PID2019-106519RB-I00 as well as BCAM Severo Ochoa accreditation SEV-

2017-0718. This work was supported by the BERC 2018-2021 Program, ELKARTEK Programme, grants KK-2020/00049 and KK-2020/00008, and "AI in BCAM, EXP. 2019/00432" funded by the Basque Government. The SGI/IZO-SGIker UPV/EHU, the i2BASQUE academic network, the HPC-Europa3 grant HPC17ERWTO, the DIPC Supercomputing Center and the Barcelona Supercomputer Center (activities QS-2020-1-0008 and QS-2020-2-0001) are acknowledged for computational resources.

Contributions

M.R.B. wrote the manuscript, F.G.D. set up and run the simulations, J.C. proposed the system and provided insights to link experimental and simulated data, and E.A. conceived the simulations and proposed the tuning recipe for the GSHMC algorithm. F.A. and P.R. prepared the membranes and performed the mechanical and electrochemical analysis. All authors analyzed the results and contributed in revising the manuscript.

Competing interests

The authors have no competing interests.

References

(1) Janek, J.; Zeier, W. G. A solid future for battery development. Nature Energy **2016**, 1, 16141.

(2) Boaretto, N.; Garbayo, I.; Valiyaveettil-SobhanRaj, S.; Quintela, A.; Li, C.; Casas-Cabanas, M.; Aguesse, F. Lithium solid-state batteries: State-of-the-art and challenges for materials, interfaces and processing. Journal of Power Sources **2021**, 229919.

(3) Placke, T.; Kloepsch, R.; Dühnen, S.; Winter, M. Lithium ion, lithium metal, and alter-

native rechargeable battery technologies: the odyssey for high energy density. Journal of Solid State Electrochemistry **2017**, 21, 1939–1964.

(4) Famprikis, T.; Canepa, P.; Dawson, J. A.; Islam, M. S.; Masquelier, C. Fundamentals of inorganic solid-state electrolytes for batteries. Nature Materials **2019**, 18, 1278–1291.

(5) Thangadurai, V.; Narayanan, S.; Pinzaru, D. Garnet-Type Solid-State Fast Li Ion Conductors for Li Batteries: Critical Review. Chemical Society Reviews **2014**, 43, 4714–4727.

(6) Aguesse, F.; Manalastas, W.; Buannic, L.; Lopez del Amo, J. M.; Singh, G.; Llordés, A.; Kilner, J. Investigating the Dendritic Growth during Full Cell Cycling of Garnet Electrolyte in Direct Contact with Li Metal. ACS Applied Materials & Interfaces **2017**, 9, 3808–3816.

(7) Hofstetter, K.; Samson, A. J.; Narayanan, S.; Thangadurai, V. Present understanding of the stability of Li-stuffed garnets with moisture, carbon dioxide, and metallic lithium. Journal of Power Sources **2018**, 390, 297 – 312.

(8) Vervaeke, M.; Calabrese, G. Prospective design in the automotive sector and the trajectory of the Bluecar project: An electric car sharing system. International Journal of Vehicle Design **2015**, 68, 245.

(9) Yang, T.; Zheng, J.; Cheng, Q.; Hu, Y.-Y.; Chan, C. K. Composite Polymer Electrolytes with $Li_7La_3Zr_2O_{12}$ Garnet-Type Nanowires as Ceramic Fillers: Mechanism of Conductivity Enhancement and Role of Doping and Morphology. ACS Applied Materials & Interfaces **2017**, 9, 21773–21780.

(10) Xu, H.; Chien, P.-H.; Shi, J.; Li, Y.; Wu, N.; Liu, Y.; Hu, Y.-Y.; Goodenough, J. B. High-performance all-solid-state batteries enabled by salt bonding to perovskite in poly(ethylene oxide). Proceedings of the National Academy of Sciences **2019**, 116, 18815–18821.

(11) Wu, N.; Chien, P.-H.; Qian, Y.; Li, Y.; Xu, H.; Grundish, N. S.; Xu, B.; Jin, H.; Hu, Y.-Y.; Yu, G.; Goodenough, J. B. Enhanced Surface Interactions Enable Fast Li^+ Conduction in Oxide/Polymer Composite Electrolyte. Angewandte Chemie International Edition **2020**, 59, 4131–4137.

(12) Zheng, J.; Hu, Y.-Y. New Insights into the Compositional Dependence of Li-Ion Transport in Polymer-Ceramic Composite Electrolytes. ACS Applied Materials & Interfaces **2018**, 10, 4113–4120, PMID: 29303244.

(13) Zagórski, J.; López del Amo, J. M.; Cordill, M. J.; Aguesse, F.; Buannic, L.; Llordés, A. Garnet-Polymer Composite Electrolytes: New Insights on Local Li-Ion Dynamics and Electrodeposition Stability with Li Metal Anodes. ACS Applied Energy Materials **2019**, 2, 1734–1746.

(14) Wang, Y.; Ju, J.; Dong, S.; Yan, Y.; Jiang, F.; Cui, L.; Wang, Q.; Han, X.; Cui, G. Facile Design of Sulfide-Based all Solid-State Lithium Metal Battery: In Situ Polymerization within Self-Supported Porous Argyrodite Skeleton. Advanced Functional Materials **2021**, n/a, 2101523.

(15) Yan, Y.; Ju, J.; Dong, S.; Wang, Y.; Huang, L.; Cui, L.; Jiang, F.; Wang, Q.; Zhang, Y.; Cui, G. In Situ Polymerization Permeated Three-Dimensional Li^+-Percolated Porous Oxide Ceramic Framework Boosting All Solid-State Lithium Metal Battery. Advanced Science **2021**, 8, 2003887.

(16) Qian, X.; Gu, N.; Cheng, Z.; Yang, X.; Wang, E.; Dong, S. Impedance study of $(PEO)_{10}LiClO_4$-Al_2O_3 composite polymer electrolyte with blocking electrodes. Electrochimica Acta **2001**, 46, 1829–1836.

(17) Kim, J.-W.; Ji, K.-S.; Lee, J.-P.; Park, J.-W. Electrochemical characteristics of two types of PEO-based composite electrolyte with functional SiO_2. Journal of Power

Sources **2003**, 119-121, 415–421, Selected papers presented at the 11th International Meeting on Lithium Batteries.

(18) Capuano, F.; Croce, F.; Scrosati, B. Composite Polymer Electrolytes. Journal of The Electrochemical Society **1991**, 138, 1918–1922.

(19) Wieczorek, W.; Zalewska, A.; Raducha, D.; Florjańczyk, Z.; Stevens, J. R. Composite Polyether Electrolytes with Lewis Acid Type Additives. The Journal of Physical Chemistry B **1998**, 102, 352–360.

(20) Ganapatibhotla, L. V. N. R.; Maranas, J. K. Interplay of Surface Chemistry and Ion Content in Nanoparticle-Filled Solid Polymer Electrolytes. Macromolecules **2014**, 47, 3625–3634.

(21) Liu, W.; Lee, S. W.; Lin, D.; Shi, F.; Wang, S.; Sendek, A. D.; Cui, Y. Enhancing ionic conductivity in composite polymer electrolytes with well-aligned ceramic nanowires. Nature Energy **2017**, 2, 17035.

(22) Li, Z.; Huang, H.-M.; Zhu, J.-K.; Wu, J.-F.; Yang, H.; Wei, L.; Guo, X. Ionic Conduction in Composite Polymer Electrolytes: Case of PEO:Ga-LLZO Composites. ACS Applied Materials & Interfaces **2019**, 11, 784–791.

(23) Choi, J.-H.; Lee, C.-H.; Yu, J.-H.; Doh, C.-H.; Lee, S.-M. Enhancement of ionic conductivity of composite membranes for all-solid-state lithium rechargeable batteries incorporating tetragonal $Li_7La_3Zr_2O_{12}$ into a polyethylene oxide matrix. Journal of Power Sources **2015**, 274, 458–463.

(24) Mogurampelly, S.; Ganesan, V. Effect of Nanoparticles on Ion Transport in Polymer Electrolytes. Macromolecules **2015**, 48, 2773–2786.

(25) Mogurampelly, S.; Ganesan, V. Influence of nanoparticle surface chemistry on ion transport in polymer nanocomposite electrolytes. Solid State Ionics **2016**, 286, 57–65.

(26) Li, Y.; Zhao, Y.; Cui, Y.; Zou, Z.; Wang, D.; Shi, S. Screening polyethylene oxide-based composite polymer electrolytes via combining effective medium theory and Halpin-Tsai model. Computational Materials Science **2018**, 144, 338 – 344.

(27) Ebadi, M.; Costa, L. T.; Araujo, C. M.; Brandell, D. Modelling the Polymer Electrolyte/Li-Metal Interface by Molecular Dynamics simulations. Electrochimica Acta **2017**, 234, 43 – 51.

(28) Zhang, H.; Chen, F.; Carrasco, J. Nanoscale modelling of polymer electrolytes for rechargeable batteries. Energy Storage Materials **2021**, 36, 77–90.

(29) Akhmatskaya, E.; Reich, S. GSHMC: An Efficient Method for Molecular Simulation. J. Comput. Phys. **2008**, 227, 4934 – 4954.

(30) Akhmatskaya, E.; Fernández-Pendás, M.; Radivojević, T.; Sanz-Serna, J. M. Adaptive Splitting Integrators for Enhancing Sampling Efficiency of Modified Hamiltonian Monte Carlo Methods in Molecular Simulation. Langmuir **2017**, 33, 11530–11542.

(31) Dutta, R. C.; Bhatia, S. K. Structure and Gas Transport at the Polymer-Zeolite Interface: Insights from Molecular Dynamics Simulations. ACS Applied Materials & Interfaces **2018**, 10, 5992–6005, PMID: 29350032.

(32) Semino, R.; Ramsahye, N. A.; Ghoufi, A.; Maurin, G. Microscopic Model of the Metal-Organic Framework/Polymer Interface: A First Step toward Understanding the Compatibility in Mixed Matrix Membranes. ACS Applied Materials & Interfaces **2016**, 8, 809–819, PMID: 26653765.

(33) Gupta, A.; Sakamoto, J. Controlling Ionic Transport through the PEO-LiTFSI/LLZTO Interface. The Electrochemical Society Interface **2019**, 28, 63–69.

(34) García Daza, F. A.; Bonilla, M. R.; Llordés, A.; Carrasco, J.; Akhmatskaya, E. Atom-

istic Insight into Ion Transport and Conductivity in Ga/Al-Substituted $Li_7La_3Zr_2O_{12}$ Solid Electrolytes. ACS Applied Materials & Interfaces **2019**, 11, 753–765.

(35) Jorgensen, W. L.; Maxwell, D. S.; Tirado-Rives, J. Development and Testing of the OPLS All-Atom Force Field on Conformational Energetics and Properties of Organic Liquids. Journal of the American Chemical Society **1996**, 118, 11225–11236.

(36) Meabe, L.; Peña, S. R.; Martinez-Ibañez, M.; Zhang, Y.; Lobato, E.; Manzano, H.; Armand, M.; Carrasco, J.; Zhang, H. Insight into the Ionic Transport of Solid Polymer Electrolytes in Polyether and Polyester Blends. The Journal of Physical Chemistry C **2020**, 124, 17981–17991.

(37) Köddermann, T.; Paschek, D.; Ludwig, R. Molecular Dynamic Simulations of Ionic Liquids: A Reliable Description of Structure, Thermodynamics and Dynamics. ChemPhysChem **2007**, 8, 2464–2470.

(38) Brooks, D. J.; Merinov, B. V.; Goddard, W. A.; Kozinsky, B.; Mailoa, J. Atomistic Description of Ionic Diffusion in PEO-LiTFSI: Effect of Temperature, Molecular Weight, and Ionic Concentration. Macromolecules **2018**, 51, 8987–8995.

(39) Brogioli, D.; Langer, F.; Kun, R.; La Mantia, F. Space-Charge Effects at the $Li_7La_3Zr_2O_{12}$/Poly(ethylene oxide) Interface. ACS Applied Materials & Interfaces **2019**, 11, 11999–12007.

(40) Horowitz, A. A Generalized Guided Monte Carlo Algorithm. Physics Letters B **1991**, 268, 247–252.

(41) Escribano, B.; Akhmatskaya, E.; Mujika, I. Combining Stochastic and Deterministic Approaches within High Efficiency Molecular Simulations. Cent. Eur. J. Math. **2013**, 11, 787 – 799.

(42) Fernández-Pendás, M.; Akhmatskaya, E.; Sanz-Serna, J. Adaptive Multi-Stage Integrators for Optimal Energy Conservation in Molecular Simulations. J. Comput. Phys. **2016**, 327, 434 – 449.

(43) Pronk, S.; Páll, S.; Schulz, R.; Larsson, P.; Bjelkmar, P.; Apostolov, R.; Shirts, M. R.; Smith, J. C.; Kasson, P. M.; van der Spoel, D.; Hess, B.; Lindahl, E. GROMACS 4.5: a High-Throughput and Highly Parallel Open Source Molecular Simulation Toolkit. Bioinformatics **2013**, 29, 845–854.

(44) Bonilla, M. R.; García Daza, F. A.; Carrasco, J.; Akhmatskaya, E. Exploring Li-ion Conductivity in Cubic, Tetragonal and Mixed-Mhase Al-Substituted $Li_7La_3Zr_2O_{12}$ using Atomistic Simulations and Effective Medium Theory. Acta Mater. **2019**, 175, 426 – 435.

(45) Martínez, L.; Andrade, R.; Birgin, E. G.; Martínez, J. M. PACKMOL: A package for Building Initial Configurations for Molecular Dynamics Simulations. J. Comput. Phys. **2009**, 30, 2157–2164.

(46) Parrinello, M.; Rahman, A. Polymorphic Transitions in Single Crystals: A New Molecular Dynamics Method. J. Appl. Phys. **1981**, 52, 7182–7190.

(47) Hess, B. P-LINCS: A Parallel Linear Constraint Solver for Molecular Simulation. J. Chem. Theory Comput. **2008**, 4, 116–122.

(48) Bernuy-López, C.; Manalastas, W.; López del Amo, J. M.; Aguadero, A.; Aguesse, F.; Kilner, J. A. Atmosphere Controlled Processing of Ga-Substituted Garnets for High Li-Ion Conductivity Ceramics. Chemistry of Materials **2014**, 26, 3610–3617.

(49) Buannic, L.; Orayech, B.; López Del Amo, J.-M.; Carrasco, J.; Katcho, N. A.; Aguesse, F.; Manalastas, W.; Zhang, W.; Kilner, J.; Llordés, A. Dual Substitution Strategy to Enhance Li^+ Ionic Conductivity in $Li_7La_3Zr_2O_{12}$ Solid Electrolyte. Chemistry of Materials **2017**, 29, 1769–1778.

(50) Bernuy-Lopez, C.; Manalastas, W.; Lopez del Amo, J. M.; Aguadero, A.; Aguesse, F.; Kilner, J. A. Atmosphere Controlled Processing of Ga-Substituted Garnets for High Li-Ion Conductivity Ceramics. Chemistry of Materials **2014**, 26, 3610–3617.

(51) Zheng, J.; Dang, H.; Feng, X.; Chien, P.-H.; Hu, Y.-Y. Li-ion transport in a representative ceramic-polymer-plasticizer composite electrolyte: $Li_7La_3Zr_2O_{12}$-polyethylene oxide-tetraethylene glycol dimethyl ether. J. Mater. Chem. A **2017**, 5, 18457–18463.

(52) Canepa, P.; Dawson, J. A.; Sai Gautam, G.; Statham, J. M.; Parker, S. C.; Islam, M. S. Particle Morphology and Lithium Segregation to Surfaces of the $Li_7La_3Zr_2O_{12}$ Solid Electrolyte. Chemistry of Materials **2018**, 30, 3019–3027.

(53) PoÅijyczka, K.; Marzantowicz, M.; Dygas, J.; Krok, F. Ionic Conductivity And Lithium Transference Number Of Poly(Ethylene Oxide):LiTFSI System. Electrochimica Acta **2017**, 227, 127–135.

(54) Semenov, A. N.; Bonet-Avalos, J.; Johner, A.; Joanny, J. F. Adsorption of Polymer Solutions onto a Flat Surface. Macromolecules **1996**, 29, 2179–2196.

(55) Legon, A. C.; Millen, D. J. Angular geometries and other properties of hydrogen-bonded dimers: a simple electrostatic interpretation of the success of the electron-pair model. Chem. Soc. Rev. **1987**, 16, 467–498.

(56) Alexander, S., Adsorption of chain molecules with a polar head a scaling description. J. Phys. France **1977**, 38, 983–987.

(57) de Gennes, P. Polymers at an interface; a simplified view. Advances in Colloid and Interface Science **1987**, 27, 189–209.

(58) Lee, H.; de Vries, A. H.; Marrink, S.-J.; Pastor, R. W. A Coarse-Grained Model for Polyethylene Oxide and Polyethylene Glycol: Conformation and Hydrodynamics. The Journal of Physical Chemistry B **2009**, 113, 13186–13194, PMID: 19754083.

(59) Brittain, W. J.; Minko, S. A structural definition of polymer brushes. Journal of Polymer Science Part A: Polymer Chemistry **2007**, 45, 3505–3512.

(60) Leijonmarck, S.; Carlson, T.; Lindbergh, G.; Asp, L.; Maples, H.; Bismarck, A. Solid polymer electrolyte-coated carbon fibres for structural and novel micro batteries. Composites Science and Technology **2013**, 89, 149–157.

(61) Dong, B. X.; Bennington, P.; Kambe, Y.; Sharon, D.; Dolejsi, M.; Strzalka, J.; Burnett, V. F.; Nealey, P. F.; Patel, S. N. Nanothin film conductivity measurements reveal interfacial influence on ion transport in polymer electrolytes. Mol. Syst. Des. Eng. **2019**, 4, 597–608.

(62) Borodin, O.; Smith, G. D.; Douglas, R. Force Field Development and MD Simulations of Poly(ethylene oxide)/LiBF4 Polymer Electrolytes. The Journal of Physical Chemistry B **2003**, 107, 6824–6837.

(63) Borodin, O.; Smith, G. D. Mechanism of Ion Transport in Amorphous Poly(ethylene oxide)/LiTFSI from Molecular Dynamics Simulations. Macromolecules **2006**, 39, 1620–1629.

(64) Diddens, D.; Heuer, A.; Borodin, O. Understanding the Lithium Transport within a Rouse-Based Model for a PEO/LiTFSI Polymer Electrolyte. Macromolecules **2010**, 43, 2028–2036.

(65) Maitra, A.; Heuer, A. Cation Transport in Polymer Electrolytes: A Microscopic Approach. Phys. Rev. Lett. **2007**, 98, 227802.

(66) Kienberger, F.; Pastushenko, V. P.; Kada, G.; Gruber, H. J.; Riener, C.; Schindler, H.; Hinterdorfer, P. Static and Dynamical Properties of Single Poly(Ethylene Glycol) Molecules Investigated by Force Spectroscopy. Single Molecules **2000**, 1, 123–128.

(67) Liu, P.; Harder, E.; Berne, B. J. On the Calculation of Diffusion Coefficients in Confined Fluids and Interfaces with an Application to the Liquid-Vapor Interface of Water. The Journal of Physical Chemistry B **2004**, 108, 6595–6602.

(68) Hanson, B.; Pryamitsyn, V.; Ganesan, V. Mechanisms Underlying Ionic Mobilities in Nanocomposite Polymer Electrolytes. ACS Macro Letters **2013**, 2, 1001–1005.

(69) Balberg, I. Universal percolation-threshold limits in the continuum. Phys. Rev. B **1985**, 31, 4053–4055.

(70) Archie, G. The Electrical Resistivity Log as an Aid in Determining Some Reservoir Characteristics. Transactions of the AIME **1942**, 146, 54–62.

(71) Hashin, Z.; Shtrikman, S. A Variational Approach to the Theory of the Effective Magnetic Permeability of Multiphase Materials. Journal of Applied Physics **1962**, 33, 3125–3131.

(72) Tobochnik, J.; Laing, D.; Wilson, G. Random-walk calculation of conductivity in continuum percolation. Physical Review A **1990**, 41, 3052–3058.

(73) Pal, R. Permeation models for mixed matrix membranes. Journal of Colloid and Interface Science **2008**, 317, 191–198.

(74) Pan, Y.; Weng, G. J.; Meguid, S. A.; Bao, W. S.; Zhu, Z.-H.; Hamouda, A. M. S. Percolation threshold and electrical conductivity of a two-phase composite containing randomly oriented ellipsoidal inclusions. Journal of Applied Physics **2011**, 110, 123715.

(75) Rubinstein, M. Polymer Physics; Oxford University Press, 2003.

(76) Nan, C.-W.; Smith, D. M. A.c. electrical properties of composite solid electrolytes. Materials Science and Engineering: B **1991**, 10, 99–106.

(77) Kirkpatrick, S. Percolation and Conduction. Reviews of Modern Physics **1973**, 45, 574–588, cited By 4086.

(78) Xu, W.; Jia, M.; Gong, Z. Thermal conductivity and tortuosity of porous composites considering percolation of porous network: From spherical to polyhedral pores. Composites Science and Technology **2018**, 167, 134–140.

(79) Stauffer, D.; Aharony, A. Introduction To Percolation Theory: Second Edition. **1992**,

(80) Vassileva, E.; Friedrich, K. Epoxy/alumina nanoparticle composites. I. Dynamic mechanical behavior. Journal of Applied Polymer Science **2003**, 89, 3774–3785.

Graphical TOC Entry